Source contribution to ozone pollution during June 2021 in Arizona: Insights from WRF-Chem tagged O_3 and CO

Yafang Guo[1,2], Mohammad Amin Mirrezaei[1], Armin Sorooshian[1,3], Avelino F. Arellano[1,3]

[1] *Department of Hydrology and Atmospheric Sciences*, *The University of Arizona, Tucson, AZ, USA*

[2] *Sonoma Technology, 1450 N. McDowell Blvd., Suite 200, Petaluma, CA, USA*

[3] *Department of Chemical and Environmental Engineering*, *The University of Arizona, Tucson, AZ, USA*

Corresponding to: Avelino F. Arellano (afarellano@arizona.edu)

Abstract. This study reports the contribution of fire emissions on ozone (O_3) pollution in Arizona compared to local and regional anthropogenic emissions. Using the WRF-Chem modeling system with different O_3 and CO tags, we quantified the contributions of these emissions to O_3 levels during June 2021, a period when the region was experiencing both drought conditions and extreme heat. Our findings indicate that background O_3 levels accounted for about 50% of the total O_3, with local anthropogenic emissions contributing between 24% and 40%. During the peak smoky time period, fire-contributed O_3 was significant across the Phoenix metropolitan area, ranging from 5 to 23 ppb or 5% to 21 % of total O_3 levels, with an average of 15 ppb or 15%. These O_3 fire tags are compared with a model sensitivity test that was conducted with fire emissions excluded, which showed strong agreement on the spatiotemporal pattern of O_3 due to fire emissions, although the magnitude of the contribution is underestimated by a factor of 1.4. This further demonstrates that wildfires exacerbate O_3 exceedances over urban areas. Our analysis also showed that the O_3 levels in Yuma are significantly influenced by transboundary pollution from California and Mexico, whereas Phoenix's O_3 levels are mainly driven by local anthropogenic emissions, with much smaller contributions from external sources during the study period. Consistent with previous reports, our findings highlight the role of wildfires and regional emissions in confounding the assessment of local O_3 pollution in urban environments, especially during dry and extremely hot summer in semi-arid/arid regions.

1. Introduction

Ozone (O_3) pollution remains a pressing environmental and public health concern, especially in regions prone to wildfire activity (Jaffe et al., 2020; Jaffe and Wigder, 2012; Abatzoglou and Williams, 2016). Elevated O_3 levels can lead to a range of respiratory issues, cardiovascular problems, and other health complications, underscoring the importance of identifying and mitigating the sources of O_3 exceedances (Turner et al., 2016; Adhikari and Yin, 2020; Huangfu and Atkinson, 2020). Arizona, particularly the south/southeast region, which is part of the Sonoran Desert and characterized by unique meteorological conditions and susceptibility to wildfires, presents a particularly challenging context for O_3 management (Betito et al., 2024; Guo et al., 2024; Miech et al., 2024; Sorooshian et al., 2024). During wildfire seasons, the complex interplay between local emissions, wildfire smoke, and meteorological factors contributes to significant O_3 exceedances, posing risks to both human health and ecological systems (Jaffe and Wigder, 2012; Jaffe et al., 2013; Selimovic et al., 2020).

Wildfires can significantly impact urban O_3 levels by releasing large quantities of pollutants that act as precursors to O_3 formation, including volatile organic compounds (VOCs) and nitrogen oxides (NO_x) (Andreae, 2019; Akagi et al., 2012). The pollutants can be transported over long distances by wind, affecting urban air quality far from the fire source and combining with local emissions to exacerbate O_3 pollution (Xu et al., 2021; Jin et al., 2023; Jaffe and Wigder, 2012; Ninneman and Jaffe, 2021). In addition to O_3, wildfire smoke leads to an increase in other atmospheric oxidants, such as hydroxyl radicals (OH) and hydroperoxyl radicals (HO_2), while reducing NO_2 photolysis rates due to the shading effect of smoke plumes (Buysse et al., 2019). This shading effect reduces the amount of sunlight available for the photolysis of NO_2, which is a crucial step in O_3 formation. During wildfire events, stagnant air conditions often prevail in urban regions, preventing the dispersion of pollutants and allowing them to accumulate. For example, temperature inversions, which are more common during these events, trap pollutants near the ground, leading to higher concentrations of O_3 and other harmful substances (Alonso-Blanco et al., 2018; Burke et al., 2023; Jaffe et al., 2020; Xu et al., 2021).

Besides O_3 and its precursors, carbon monoxide (CO) is emitted directly from wildfires. During a wildfire, the high temperature during its flaming phase causes rapid oxidation of carbon-containing

materials, but not all the carbon is fully oxidized to carbon dioxide (CO_2) during its (lower temperature) smoldering phase (Yokelson et al., 2003; Urbanski et al., 2008). CO emissions from wildfires can have far-reaching impacts, as CO is a relatively long-lived gas in the atmosphere, with a typical lifetime of several weeks to a few months. This is facilitated as well by associated plume rise especially during the fire's flaming phase.

Case studies, such as during various episodes of California wildfires, have demonstrated significant increases in urban O_3 levels, affecting cities far from the fire areas (Xu et al., 2021; Jin et al., 2023; Mcclure and Jaffe, 2018). Understanding the specific contributions of different emission sources to O_3 pollution during wildfire events is crucial for developing effective air quality management strategies. Regional and local O_3 levels are influenced by local production, in addition to regional and long-range transport of O_3 and its precursors. Anthropogenic activities, such as fossil fuel combustion by vehicles, industry, and power plants, as well as the natural biogenic emissions, are the most significant sources of NO_x and VOCs. When wildfires contribute additional NO_x and VOCs to the atmosphere, the overall levels of ground-level O_3 can rise dramatically as these plumes penetrate into urban areas, further degrading air quality (Pfister et al., 2006).

Source attribution techniques offer an alternative perspective to quantify the primary contributors to enhanced O_3 levels during smoky periods by identifying the contributions of specific sources and regions, such as anthropogenic, fire, and biogenic emissions, regional and international transport and stratospheric transport. In general, there are two main modeling approaches for O_3 source attribution or source apportionment: 1) model sensitivity experiments; 2) species tagging methods (Wang et al., 2009; Kwok et al. 2015; Clappier et al., 2017; Mertens et al., 2018; Butler et al., 2018; Thunis et al., 2019; Mertens et al., 2020). The latter modeling approach tracks O_3 formation by tagging precursors from particular source types and areas throughout the model simulation, providing a direct attribution of modeled O_3 levels to these sources. The tagging technique entails modifying the model's source code to incorporate tracers into the chemistry mechanism. Models of atmospheric chemistry and transport that have implemented a tagging technique to perform O_3 source attribution include among others the Community Multiscale Air Quality (CMAQ) model with a new version of Integrated Source Apportionment Method (ISAM) (De La Paz et al., 2024; Shu et al., 2023), a submodel called TAGGING in the EMAC (European

Centre for Medium-Range Weather Forecasts – Hamburg (ECHAM)/Modular Earth Submodel System (MESSy) (Grewe et al., 2017), the global Model for Ozone and Related chemical Tracers (MOZART- 4) (Emmons et al., 2012), the Nested Air Quality Prediction Model System (NAQPMS) (Zhang et al., 2020), CAM4-chem (Community Atmosphere Model version 4 with chemistry) within the Community Earth System Model (CESM) (Butler et al., 2018; Butler et al., 2020; Li et al., 2023; Nalam et al., 2024), the University of California Davis/Caltech air quality model (Zhao et al. 2022), the global chemical transport model (CTM) with assimilated meteorological observations from the Goddard Earth Observing System (GEOS-Chem) (Wang et al., 1998; Zhang et al., 2008; Whaley et al., 2015), and the Weather Research and Forecasting model coupled with Chemistry (WRF-Chem) (Pfister et al., 2013; Gao et al. 2016; Lupaşcu and Butler, 2019; Lupaşcu et al., 2022).

Typical model sensitivity analysis to determine the impact of a particular process (like fire) on target variables (like O_3) are usually conducted in practice as a suite of process-denial experiments and/or a series of model simulations with brute-force incremental changes on particular parameters or input datasets, along with developing model forward (decoupled direct method) and backward (adjoint) algorithms for sensitivity to emission calculations. Here, differences in simulated O_3 with and without fire emissions is interpreted to be the contribution of fire to modeled O_3 abundance. Unlike the tagging method, it utilizes the current model as is, without needing modifications. Models (and algorithms) that are used to predict how O_3 responds to changes in specific sources of emissions include among others those using WRF-SMOKE-CAMx (SMOKE: Sparse Matrix Operator Kernel Emissions model; CAMx: Comprehensive Air quality Model with extensions) (Zhang et al., 2017, Goldberg et al. 2016), WRF-Chem (Li et al., 2015), High-Order Decoupled Direct Method in Three Dimensions (HDDM-3D) (e.g., Cohan et al., 2005), CMAQ (Yeganeh et al., 2024; Collet et al., 2014, Hakami et al., 2007), STEM (Hakami et al., 2006), and climate chemistry model (E39C) (Grewe et al., 2012; Grewe et al., 2010).

These recent model and algorithm developments have shown the importance of integrating sophisticated modeling approaches and comprehensive data analysis to help better inform policies aimed at reducing O_3 pollution and its associated health impacts. Building on the work of Lupaşcu and Butler (2019) and Emmons et al. (2012), this study employs the tagging technique within the WRF-Chem modeling system to investigate the sources contributing to O_3 exceedances during a

recent Arizona wildfire season, particularly examining the impacts of fires on O_3 levels. By utilizing this advanced modeling framework, our objective is to untangle the contributions of wildfire emissions, local anthropogenic activities, and regional transport to urban O_3 pollution. We assess this tagging approach by also conducting sensitivity experiments using the WRF-Chem model configuration by excluding fire emissions (i.e., zero-out emission scenario). Our focus is on June 2021 in Arizona, a period marked by multiple active wildfires and high O_3 concentrations. Arizona's distinctive environmental and atmospheric conditions, characterized by arid and semi-arid landscapes, extreme heat, and limited precipitation, create unique challenges for understanding wildfire behavior, air quality, and atmospheric chemistry. The dry summer and monsoon summer seasons lead to significant shifts in the O_3 chemical regime (Greenslade et al., 2024), as the monsoon introduces additional moisture, which influences both wildfire smoke dynamics and overall atmospheric processes. Additionally, Arizona's urban pollution island, particularly over Phoenix, differs from those in California due to its unique geographic setting. Phoenix, as the largest city in Arizona, is surrounded by vast, undeveloped desert, creating a "sky island" effect that intensifies the urban heat dome. This heat island effect, coupled with the region's arid climate, presents distinct challenges for understanding the interactions between urban pollution and wildfire emissions. In this study, we focus on two cases where Phoenix was significantly impacted by wildfire smoke. The findings from this research offer valuable insights that can be applied to other arid regions, such as parts of the Middle East, Australia, and northern Africa, where similar environmental conditions exist. This broader applicability enhances our understanding of the impacts of wildfires in arid environments, particularly in the context of climate change.

Section 2 presents the observational datasets from ground-based Environmental Protection Agency's Air Quality System (EPA AQS) sites and satellites, alongside the model setup. Section 3 begins with a detailed introduction of the selected cases, followed by an analysis of comprehensive O_3 source apportionment. The discussion and conclusions are presented in Section 4.

2. Data and Methods

2.1 Study region and period

As mentioned, this is a case study focusing on 2021 dry summer (June) in Arizona, where most of the state falls under the arid/semi-arid region. This period was notably severe, exacerbated by a combination of prolonged drought and an intense heatwave. The state experienced one of its hottest Junes on record, with temperatures frequently exceeding 115°F (46°C), with no significant precipitation recorded. This extreme heat, combined with exceptionally dry conditions, were pivotal in the ignition and spread of multiple wildfires, leading to numerous large wildfires. In total, dozens of fires were reported across Arizona and New Mexico during this period, many sparked by lightning strikes on desert landscapes.

The Telegraph Fire, one of the largest wildfires in Arizona's history, began on 4 June 2021, near Superior, Arizona. By the time it was fully contained on 3 July 2021, the fire had burned over 180,000 acres. The burn area was located in the southernmost region of Tonto National Forest, primarily characterized by desert shrubs and grassland vegetation (USDA, 2024). The Rafael Fire started on 18 June 2021 to the southwest of Flagstaff, which prompted widespread evacuations and road closures. The Rafael Fire had burned over 38 square miles by late June in the Coconino National Forest, where evergreen shrubs were the dominate vegetation type (Conservation Biology Institute, 2024).

Figure 1 provides a comprehensive overview of the study region, focused on the Phoenix-Mesa-Scottsdale metropolitan area in Arizona, with Phoenix as the principal city. Panel (a) presents a topographic map with red dashed lines outlining the metropolitan area. The red circle marks the AQS Phoenix JLG Supersite, representing the central air quality monitoring location. In addition, red curves delineate the O_3 nonattainment area, which is of regulatory importance due to specific air quality management requirements. Throughout this study, "Phoenix" refers specifically to this nonattainment area, highlighting its relevance to targeted air quality strategies. The locations of the Rafael and Telegraph fires are marked with stars. The Telegraph Fire is located to the southeast of Phoenix and Rafael Fire is located to the north of Phoenix. Panel (b) of the figure illustrates the distribution of AQS monitoring sites within the nonattainment area. Each site is numbered and geolocated, offering an observational network for tracking O_3 and other air pollutants. Lists of the site locations and associated names are provided in Supplement Table S1. The spatial arrangement of monitoring sites facilitates a spatiotemporal analysis and assessment of pollutant level enhancements from wildfire smoke and other sources of emissions.

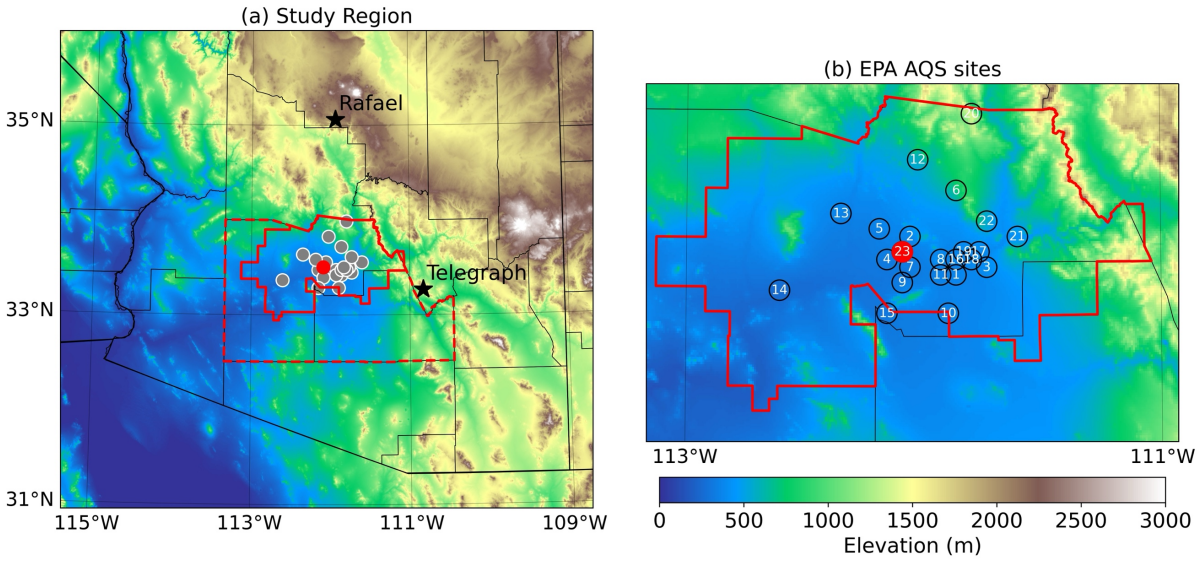

Figure 1. (a) Topographic map of the Phoenix Metropolitan Statistical Area (indicated by red dashed lines) in Arizona, showing USEPA/AQS monitoring sites as filled circles. The red circle highlights the Phoenix JLG Supersite. The O_3 nonattainment area is outlined with a solid red border. Stars mark the locations of the two largest wildfires in June 2021, the Rafael and Telegraph fires. (b) A closer view of EPA AQS sites within the nonattainment area, with sites numbered and positioned according to their geographic locations. The JLG Supersite is designated as AQS site number 23.

2.2 WRF-Chem setup

The Weather Research Forecasting with Chemistry (WRF-Chem) (Grell et al., 2005) model v4.4 is utilized here to simulate wildfire activities and study tropospheric O_3 pollution. Meteorological initial and lateral boundary conditions are supplied every six hours by the Global Forecast System (GFS) with a horizontal grid spacing of 1° and 12-km NAM (North American Mesoscale Forecast System), while chemical initial and boundary conditions are provided by the Whole Atmosphere Community Climate Model (WACCM) for chemistry (Marsh et al., 2013; Tilmes et al., 2015). Biogenic emissions are calculated online using the Model of Emissions of Gases and Aerosols from Nature (MEGAN, version 2.1) (Guenther, 2007; Guenther et al., 2006), based on the simulated meteorological conditions during the WRF-Chem runs. The anthropogenic emissions used in this study are obtained from 2017 National Emissions Inventories (NEI2017) data provided by the US EPA (https://www.epa.gov/air-emissions-inventories/2017-national-emissions-inventory-nei-data) with a 4 km grid spacing covering the U.S. and surrounding land areas.

Biomass burning emissions are calculated using the Fire Inventory from NCAR (FINNv2.5) (Wiedinmyer et al., 2023) and the online plume-rise model (Freitas et al., 2007). FINNv2.5 is based on fire counts derived from Moderate Resolution Imaging Spectroradiometer (MODIS) and Visible Infrared Imaging Radiometer Suite (VIIRS) active fire detection (Wiedinmyer et al., 2023). A summary of the model configuration, parameterization, and a comprehensive model evaluation against multiple observational and reanalysis datasets are provided in Guo et al. (2024). Note that the WRF-Chem model used in this study is coupled with the radiative effects of aerosols, such as smoke, on atmospheric temperature and photochemistry. Both direct and indirect effects of aerosols were turned on in our simulations. These effects are accounted for through radiative transfer calculations, incorporating aerosol optical properties like absorption and scattering. As a result, heavy smoke can reduce the amount of solar radiation reaching the surface, leading to surface and boundary-layer cooling. Furthermore, the attenuation of ultraviolet (UV) radiation by smoke can suppress photochemical O_3 production, influencing the atmospheric chemical environment. Our simulation period focuses on June 2021, targeting multiple wildfire activities near Phoenix as described in section 2.1.

2.3 O_3 tags and experiment design

To better understand the impacts of wildfire emissions on urban environmental settings, a species tagging technique was employed within the WRF-Chem model following recent demonstrations (Emmons et al., 2012; Gao et al. 2016; Lupaşcu and Butler, 2019; Butler et al., 2018; Butler et al., 2020). Emmons et al. (2012) first introduced a method for tracking the sources of O_3 in the troposphere using a tagging approach within various chemical transport models, specifically MOZART-4. This tagging mechanism allows for a detailed attribution of O_3 to its precursor emissions sources, providing insights into how different sources contribute to overall O_3 levels. Later on, Butler et al. (2018) applied the tagging mechanism for tracking the sources of tropospheric O_3 within the Community Earth System Model (CESM) version 1.2.2 and presented an updated version with comparison to Emmons et al. (2012). Lupaşcu and Butler (2019) then implemented the tagging mechanism within the WRF-Chem model to explore the origins of surface O_3 across Europe by distinguishing the contributions of different NO_x emission sources to O_3 concentrations in various European regions.

Following Lupaşcu and Butler (2019), here we apply the tagging technique in the WRF-Chem model to quantify the contributions of different NO_x sources by not just tagging different regions but also different types of emissions. Our tags include four main categories: 1) regions that are local and adjacent, such as Arizona, California, and Mexico; 2) emission types, including anthropogenic sources and fires; 3) tracers, including NO, NO_2, CO, and reaction products like O_3, O, and the corresponding NO_y reservoir species; and 4) background O_3 from initial and boundary O_3 levels. Note that these tracers undergo the same processes (advection, mixing, convection, chemical loss, deposition) within the continuity equation associated for each species in the model but they do not interact and affect changes in the modeled chemical system.

To implement the tagging technique in WRF-Chem, several steps must be completed before running the model. First, a tagged gas-phase chemical mechanism is created to incorporate tagged tracers and reactions representing these tagged species, as well as the production and loss of O_3 to account for the tagged NO_x emissions. The tagged O_3 in the model is represented as tracers that track its production from NO_x, as well as its subsequent transport and loss processes. Here, we assume that O_3 peaks in urban areas of Arizona during this study period (June) is under a NO_X-limited chemical regime based on our previous studies (e.g., Guo et al., 2024; Greenslade et al., 2024).This new tagged mechanism is modified from the source code of the original MOZART mechanism within the WRF-Chem model. Next, both the anthropogenic and fire emission input files are modified to include tags related to different regions. For each regional tag, such as Arizona, NO_x and CO concentrations from outside Arizona are set to zero. Finally, the tags are initialized, and their boundary conditions are determined by the WACCM model output. The advantage of using WACCM is that it provides tagged CO tracers, including global biomass burning, North American anthropogenic emissions, and continental transport from regions such as East Asia, Europe, and Africa.

Since meteorological conditions, particularly wind speed and direction, have a significant impact on wildfire activities and plume coverage, we also apply the higher resolution 12-km NAM (North American Mesoscale Forecast System) dataset as the initial and boundary conditions. Evaluations are conducted for each selected case, comparing them against two boundary conditions. The simulations featuring winds and smoke plumes that best match satellite observations are selected. To help evaluate the contribution of wildfire emissions to O_3 levels, another set of simulations is

performed by removing fire emissions. This serves as a sensitivity test for evaluating the model results with tags.

2.4 EPA AQS surface observations

To evaluate the accuracy of our model simulations, we use the surface observations from the Environmental Protection Agency's Air Quality System (EPA AQS). The AQS provides comprehensive air quality data from monitoring stations across the U.S., offering measurements of various pollutants, including O_3, particulate matter ($PM_{2.5}$ and PM_{10}), and other criteria pollutants. The hourly and daily surface in situ observations of O_3 (including MDA8), CO, NO_2, and meteorological fields such as temperature, relative humidity, and winds from the EPA AQS monitoring network are used in this study (Demerjian, 2000). A total of 23 sites within the nonattainment area were selected based on their availability of O_3 measurements during the study periods, as shown in Figure 1b. The dataset undergoes quality control procedures to filter out any erroneous or incomplete records, ensuring that only high-quality observations are used in our evaluation.

2.5 HMS smoke products

The Hazard Mapping System (HMS) smoke products provide detailed daily maps showing the geographic extent and concentration of smoke plumes across the U.S. and surrounding regions. The system integrates various satellite data sources, including the MODIS and VIIRS sensors, GOES (Geostationary Operational Environmental Satellite) imagery, to detect fire locations and estimate smoke coverage. The HMS smoke analysis has been a useful tool in monitoring wildfire impacts, supporting meteorological forecasting, and informing public safety measures related to air quality (e.g., Brey et al., 2018; Rolph et al., 2009).

The smoke products typically include three types of shapefiles: light, medium, and heavy (NOAA, 2023). Each category includes one or more shapefiles representing the smoke coverage estimated from satellite observations or images. These smoke products are used in this study to identify and select cases when Phoenix is defined as experiencing heavy smoke days.

2.6 TROPOMI satellite retrievals

The TROPOspheric Monitoring Instrument (TROPOMI) is a state-of-the-art satellite sensor onboard the European Space Agency's (ESA) Sentinel-5 Precursor (S5P) satellite, launched in

October 2017. TROPOMI actively measures tropospheric columnar atmospheric constituents including O_3, CO, NO_2, formaldehyde (HCHO). The TROPOMI dataset over Arizona has a spatial resolution of approximately 5.5 × 3.5 km² at nadir and provides daily data with an early afternoon (~12-14 PM) overpass time (Ludewig et al., 2020; Van Geffen et al., 2020). The data utilized in this research underwent a quality control process, where a quality assurance value (qa_value) greater than 0.50 was applied for HCHO and CO and a qa_value greater than 0.75 was applied for NO_2. The quality-controlled datasets were then gridded to a resolution of 0.07° × 0.07° for spatial analysis. For days with a lack of good quality data over the study domain, the data were further re-gridded to a coarser spacing of 0.2° × 0.2° to better capture the general spatial pattern of NO_2 and HCHO tropospheric columns. TROPOMI O_3 data was not used in this study due to limitations in its applicability to our research domain. The high-resolution TROPOMI O_3 product primarily represents total column O_3, which is strongly influenced by stratospheric O_3 rather than tropospheric levels (Copernicus Sentinel data processed by ESA et al., 2020a). The tropospheric column O_3 product is only available for latitudes between -20° and 20°, as it relies on the Convective Cloud Differential (CCD) method, which is most effective in regions with frequent high convective clouds (Copernicus Sentinel data processed by ESA et al., 2020b; Heue et al., 2021). This limitation excludes our study area. Additionally, the CCD method has shown stronger utility in tropical regions (Cazorla & Herrera, 2022). While TROPOMI O_3 profile data is available, calculating tropospheric columns requires additional processing and extensive validation, which is beyond the scope of this study. Furthermore, O_3 profiles do not directly represent surface O_3 levels, unlike NO_2, which has a shorter lifetime and is primarily associated with surface emissions from combustion sources.

3. Results and discussions

3.1 Case selection

Throughout June 2021, Phoenix experienced an intensified heatwave and drought conditions conducive for wildfire activity. Figure 2 presents the observed daily variations of pollutant levels for June 2021 from the EPA AQS at the Phoenix JLG Supersite compared to results from the TROPOMI satellite. Data on temperature (T) shows the heatwave began on June 12, with the daily maximum temperature reaching 43°C and remaining at least that high until June 20. The Maximum Daily 8-Hour Average Ozone (MDA8 O_3) levels were around 50-70 ppb until June 10, when O_3

began to increase, exceeding the EPA National Ambient Air Quality Standard (NAAQS) standard (70 ppb) along with elevated surface concentrations of CO and NO_2, and T. A notably high MDA8 O_3 level (100 ppb) was observed on June 15. MDA8 O_3 then decreased to below NAAQS levels on June 17 up until June 27. Surface CO levels generally followed the O_3 variation, ranging between 400-700 ppb. However, a noticeable peak in surface CO, exceeding 1000 ppb, was observed on June 11, which was not shown in the TROPOMI tropospheric column CO, while both surface and tropospheric column NO_2 levels exhibited a significant peak, indicating that emissions were mostly within the planetary boundary layer. Conversely, the discrepancies between NO_2 surface and column levels beginning June 13 suggest different sources for surface and tropospheric NO_2 and CO emissions, particularly on June 15, when MDA8 O_3 exceeded 100 ppb; surface NO_2 and CO was relatively low, while column NO_2 and CO were high. The peak period beginning June 14 of HCHO concentration was also captured by both AQS and TROPOMI observations. In Guo et al. (2024), they showed that during the period with elevated temperature (June 12-20), relative humidity is low but normal for June in Arizona. The high temperature resulted in an increase of isoprene and HCHO simultaneously.

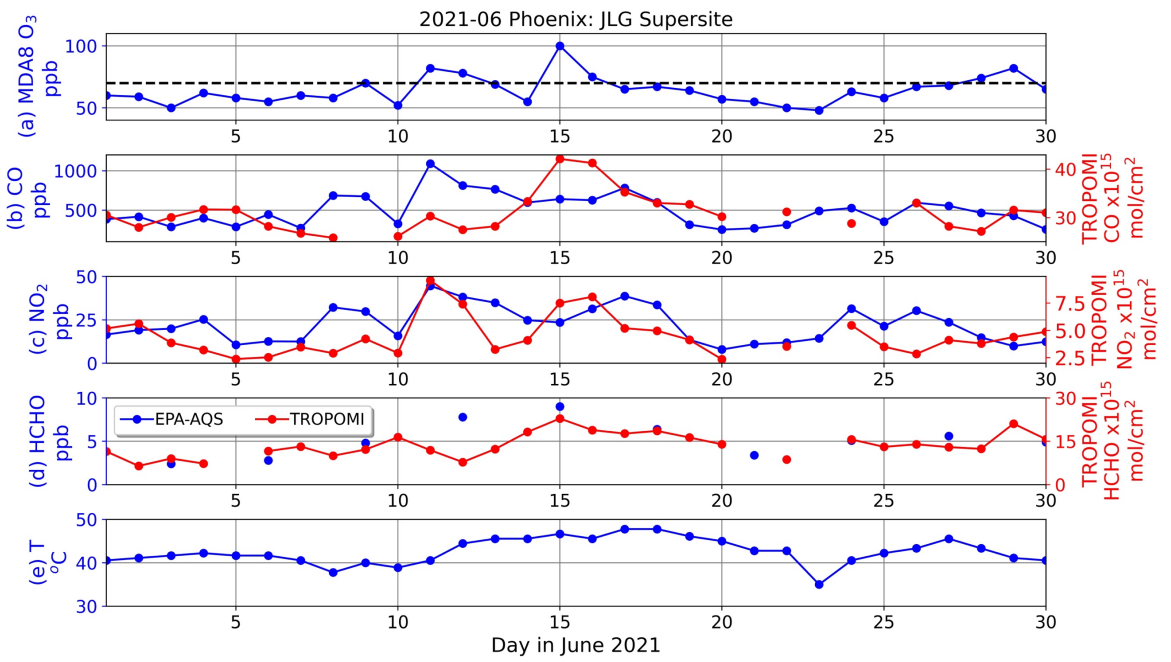

Figure 2. Observational daily variations of surface (a) MDA8 O_3, (b) CO, (c) NO_2, (d) HCHO, and (e) temperature (T) from EPA AQS at Phoenix JLG supersite (blue), as well as column (b) CO, (c) NO_2, and (d) HCHO concentrations from TROPOMI satellite (red) in June 2021. The NAAQS 2015 standard is denoted as black dash line. Note that the daily AQS CO, NO_2, and T values shown represent the daily maximum while the HCHO value is the daily mean.

As mentioned earlier, the Telegraph Fire began on June 3 and lasted for one month, while the Rafael Fire started on June 18. Guo et al. (2024) showed that in the month of June, the prevailing wind over Phoenix was mostly southwesterly, limiting the impacts of these wildfires on Phoenix to certain days when winds shifted direction and brought smoke plumes to the city. After reviewing the HMS smoke data for June 2021, we identified two smoky periods that might have potentially influenced surface O_3 concentrations over Phoenix.

The first selected case is on 15 June 2021. On this day, multiple sites within the nonattainment area observed O_3 exceedances (>70 ppb). An excessive heat warning was issued and remained in effect through the end of the week, with temperatures 10 to 15 degrees above average (Gard and Garrett, 2021). The wind shifted from southwesterly to northeasterly, bringing the Telegraph Fire plumes to Phoenix. The second case is on 26 June 2021, when smoke from the Rafael Fire spread to the north of Phoenix with a change of wind direction from southwesterly to northerly.

Shown in Figure 3 is the heavy smoke coverage from the HMS smoke products over the Phoenix area during two selected cases in June 2021, highlighting the impact of the Rafael and Telegraph fires. In Case I, on 14 June 2021, at 16:00 LT, smoke from both the active Telegraph (southeast of Phoenix) Fire spread primarily to the northeast. By 15 June 2021, at 16:20 LT, the smoke coverage had expanded significantly, with a dense plume covering central Arizona, including Phoenix. On 16 June 2021, at 11:00 LT, the dense and widespread smoke continued to affect the periphery of Phoenix. In Case II, on 25 June 2021, at 07:00 LT, smoke primarily from the Rafael Fire extends to the east, far away from Phoenix. By 26 June 2021, at 17:00 LT, the smoke plume from Rafael Fire changed direction to the south and covered the north of Phoenix. Active wildfires contributing to the smoke over Phoenix are marked with yellow stars, indicating the origin and spread direction of the smoke plumes. These two cases are selected for further modeling studies to help understand how near-range wildfires affect the Phoenix metropolitan area.

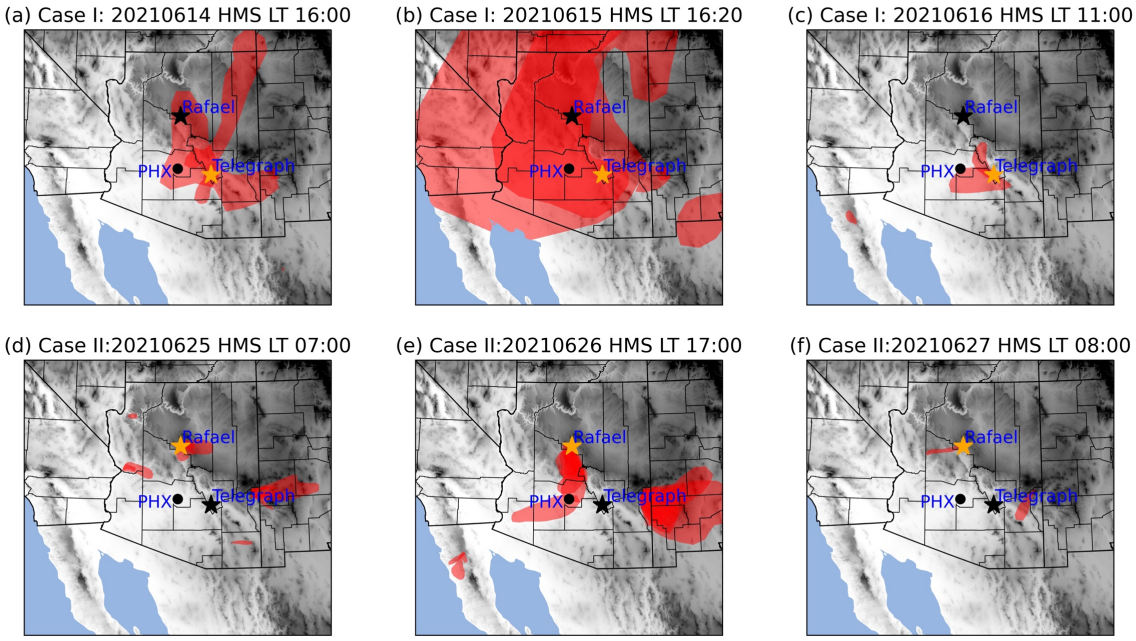

Figure 3. (a-c) Heavy smoke coverage from Hazard Mapping System (HMS) smoke products for Case I, and (d-f) for Case II over Phoenix area. The active wildfire that was accountable for the smoke over Phoenix is marked as yellow star.

In Figure S1 we present a series of screenshots from the MODIS Terra Corrected Reflectance map, overlaid with MODIS fires and thermal anomaly products, to depict wildfire activities in Arizona for the above two cases. Similar to Figure 3, the top panel illustrates Case I, focusing on the

Telegraph Fire from June 14 to 16. The bottom panel captures Case II, highlighting the Rafael Fire from June 25 to 27. Both cases show visible smoke plumes and thermal anomalies (orange color) indicating active fire regions, with the fire spreading and producing significant amounts of smoke passing Phoenix.

In addition to HMS smoke products, we show in Figure 4 the daily TROPOMI tropospheric columns of HCHO, NO_2 and CO during smoke periods for Case I over the Phoenix area. In Case I, the HCHO levels initially show low levels, with scattered low concentrations on June 13 except the east of Telegraph Fire. By June 14, there is a significant increase in HCHO, especially northeast of Phoenix, correlating with the smoke plume from the Telegraph Fire, as seen in Figure 3a. On June 15, the elevated HCHO levels were more dispersed, affecting mainly the south of Phoenix. By June 16, HCHO tropospheric column decreased to the normal levels over Phoenix. For NO_2, June 13 shows low levels with a typical urban anthropogenic emissions spatial profile. June 14 exhibits a significant increase in NO_2, particularly northeast of Phoenix, similar to the HCHO distribution. On June 15, NO_2 levels are high over a wider area, including Phoenix and the path of plumes (Figure 3b). By June 16, NO_2 levels decrease but remain elevated. A similar pattern has been observed in CO, where its high concentrations are closely correlated with HCHO, NO_2, and smoke coverage, as shown in Figure 3. The TROPOMI results for Case II are presented in Figure S2.

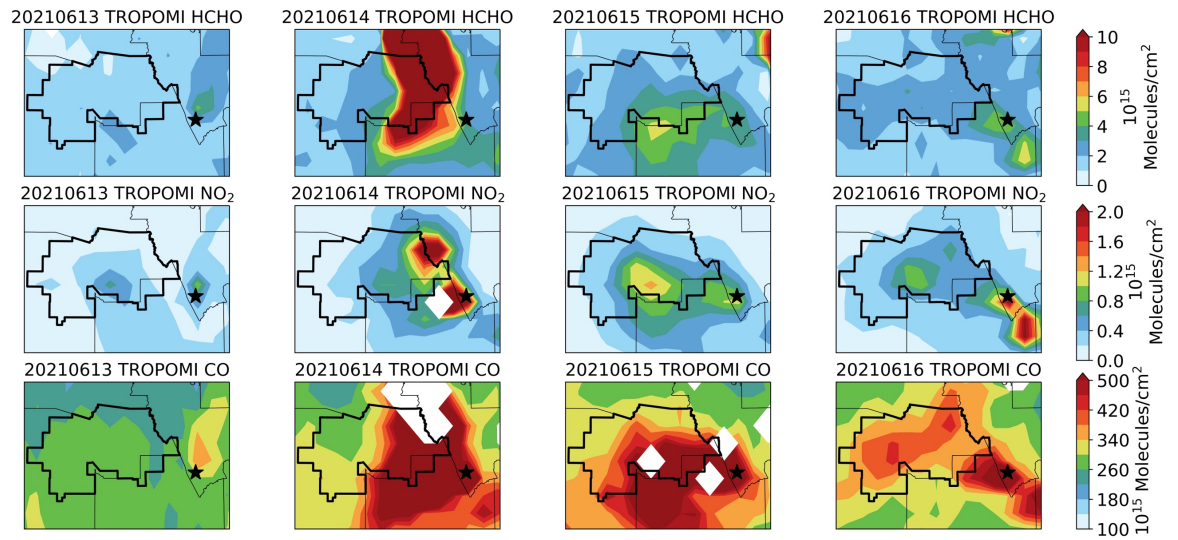

Figure 4. TROPOMI tropospheric columnar HCHO (top), NO_2 (middle), and CO (bottom) during the smoke periods for Case I over Phoenix area. The black polygon lines represent the EPA designated Phoenix-Mesa nonattainment area. The grid resolution is 0.2°. Grids without available data are marked as white space.

Similar to the TROPOMI satellite observations, we also examined the model simulation results. Figure 5 presents the WRF-Chem simulated tropospheric columnar values of HCHO, NO_2, and CO at 14:00 local time (same time as the TROPOMI observations) during the smoke periods for Case I. Comparing Figures 4 and 5, on June 13 as a pre-smoke day, the HCHO levels in the city region are comparable, with values primarily below $6x10^{15}$ molecules/cm², while the Telegraph Fire burning area reached over $10x10^{15}$ molecules/cm². This day represents a typical distribution of urban pollutants over Phoenix. By June 14, levels of HCHO, NO_2, and CO increased significantly, particularly in the southeastern part of Phoenix, although the magnitude and spatial patterns appear to differ from the satellite observations in Figure 4. On June 15, the tropospheric columnar values decreased but the wildfire signal remained significant until June 16, when the spatial pattern returned to typical conditions. Additional WRF-Chem simulated results for Case II are available in Figure S3-S4.

In summary, observations from HMS, TROPOMI, and WRF-Chem models indicate that the Telegraph Fire had a significant impact on Phoenix air quality during June 14-15. While the rise of plumes during wildfires greatly influences the columnar concentrations of pollutants by transporting smoke and emissions higher into the atmosphere, the mixing levels within the surface

or planetary boundary layer are more important to the overall air quality and pollutant distribution as the more immediate impact on public health is expected at ground-level.

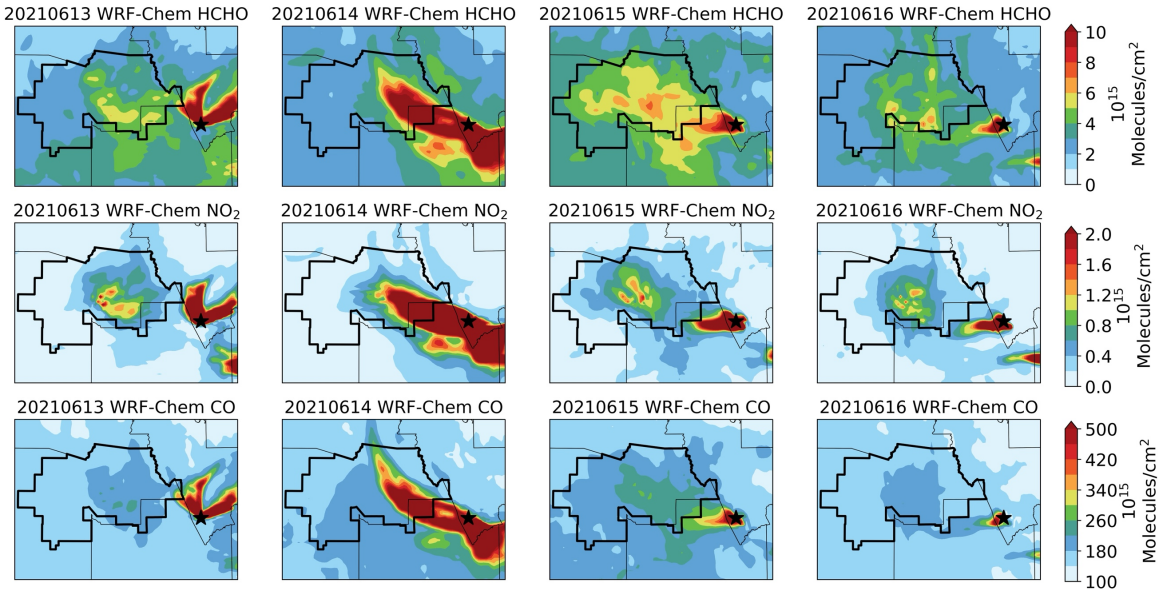

Figure 5. WRF-Chem simulated HCHO, NO_2, and CO tropospheric columns at local time 14:00 during the smoke periods for Case I over Phoenix area.

We show in Figure 6 the WRF-Chem simulated surface concentrations of HCHO, NO_2, and CO. Since each case involves two sets of simulations using GFS and NAM meteorological boundary conditions, the selection of the model results is based on an initial evaluation against AQS and satellite observations. For Case I, the results from the GFS simulations demonstrate better agreement, while for Case II, the NAM simulations show better alignment of smoke. Comparing these with the columnar levels of NO_2 and CO in Figure 5, it is evident that the extent of the smoky day on June 14, as observed from HMS and TROPOMI, is not reflected at the surface level, whereas the smoky day on June 15 is apparent in both surface and columnar concentrations. Additionally, for HCHO, increases are also observed at the surface on June 14. This discrepancy indicates that on June 14, the wildfire smoke was primarily affecting atmospheric layers aloft without significantly impacting the ground level, while on June 15, the smoke was more distributed in the lowermost troposphere, increasing the surface pollution concentrations. Model results of tropospheric column and surface HCHO, NO_2, and CO for Case II are provided for reference in the Supplement as Figures S1-S2, respectively.

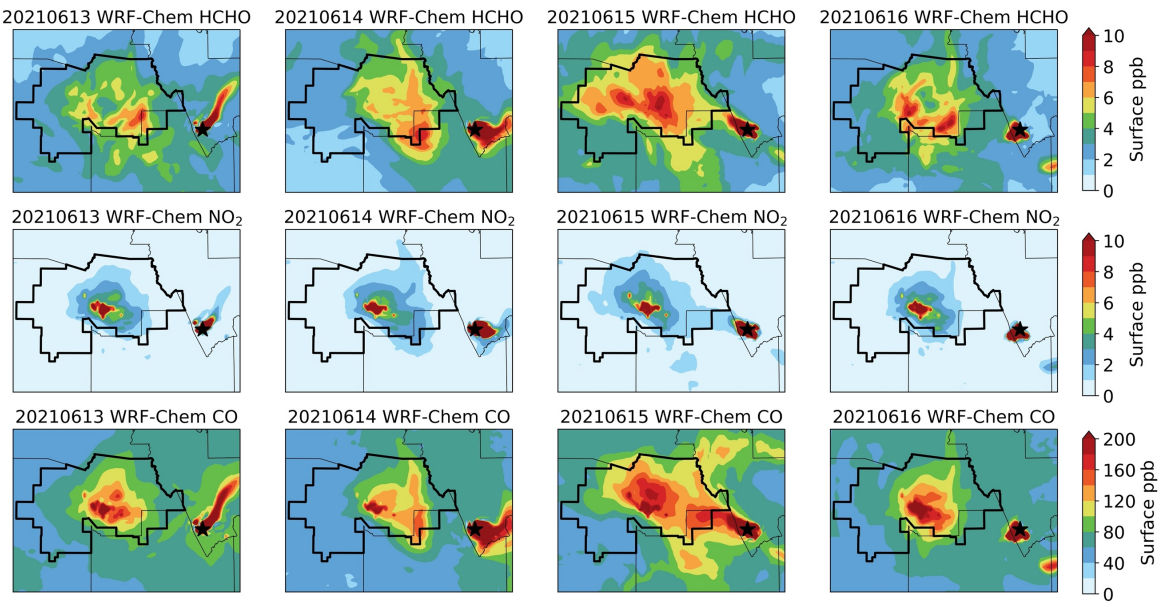

Figure 6. Same as Figure 5, but for surface concentrations.

3.2 Source attribution with tags

An extensive evaluation of the same configuration of the WRF-Chem model using the MOZART chemical mechanism, except for the tags, has been presented previously by Guo et al. (2024). Briefly, our evaluation showed a Pearson correlation coefficient (R) of 0.81 for modeled and observed O_3 over Phoenix with a mean bias (MB) of -2.9 ppb and 1.0 ppb for hourly and MDA8 O_3, respectively. For CO and NO_2, the normalized bias is 7.1% and 5.3%, respectively. The model simulations also show that surface formaldehyde-to-nitrogen dioxide ratio (FNR), which is an indicator of chemical regime affecting O_3 production varies from a VOC-limited regime in the most populated areas to a transition between VOC-limited and NOx-limited regimes throughout the metro area. For the FNR threshold, we adopt the same approach as Guo et al. (2024), following the methodology of Duncan et al. (2010), who linked the FNR with surface O_3 in model simulations. According to this framework, the sensitivity regime is defined as follows: when FNR is less than 1, it is classified as VOC-limited; values between 1 and 2 indicate a transitional regime; and an FNR greater than 2 indicates a NO_x-limited regime. Here in this study, our discussion of the model results is focused on the month of June 2021, a period marked by active wildfires over Arizona against a backdrop of not only an O_3 chemical regime that is in transition to NO_X-limited but also of drought and heat wave conditions.

We first provide an analysis of the contribution of different source regions and emission types to the monthly CO and MDA8 O_3 concentrations to understand the overall pollution sources in the State of Arizona. Then, we focus on the analysis of O_3 during smoky days by examining the two selected cases described in Section 3.1. Note that in this study, "background O_3" and "background CO" refer to the residual concentrations after subtracting contributions from tagged anthropogenic and fire emissions. For both O_3 and CO, this background includes contributions from natural sources, such as biogenic emissions (e.g., isoprene for O_3 and CO), soil and lightning NO_x for O_3, and stratospheric ozone, as well as long-range transport from both natural and anthropogenic sources. During heatwave events, background O_3 and CO can be particularly elevated due to enhanced biogenic emissions and other natural fluxes. Thus, the background levels of O_3 and CO in this context represent a combination of regional and global influences from natural sources and transported components, not solely remote anthropogenic contributions.

3.2.1 Monthly CO and O_3 extremes for June 2021

Shown in Figure 7 is an overview of CO concentrations in Arizona during June 2021, highlighting the impact of various sources on CO distribution. Each panel represents the 90th percentile for the entire month of different CO and its sources: (a) total CO, (b) background CO levels, (c) anthropogenic CO sources, (d) CO from California anthropogenic sources, (e) CO from Arizona anthropogenic sources, (f) CO from Mexico anthropogenic sources, (g) CO from Arizona wildfires, and (h) CO from Mexico wildfires. Comparing the total CO concentrations (Figure 7a) with anthropogenic CO (Figure 7c), we can see a clear signature of anthropogenic activities in cities such as Phoenix (PHX), Tucson (TUS), and Las Vegas, located in the upper left corner of the map.

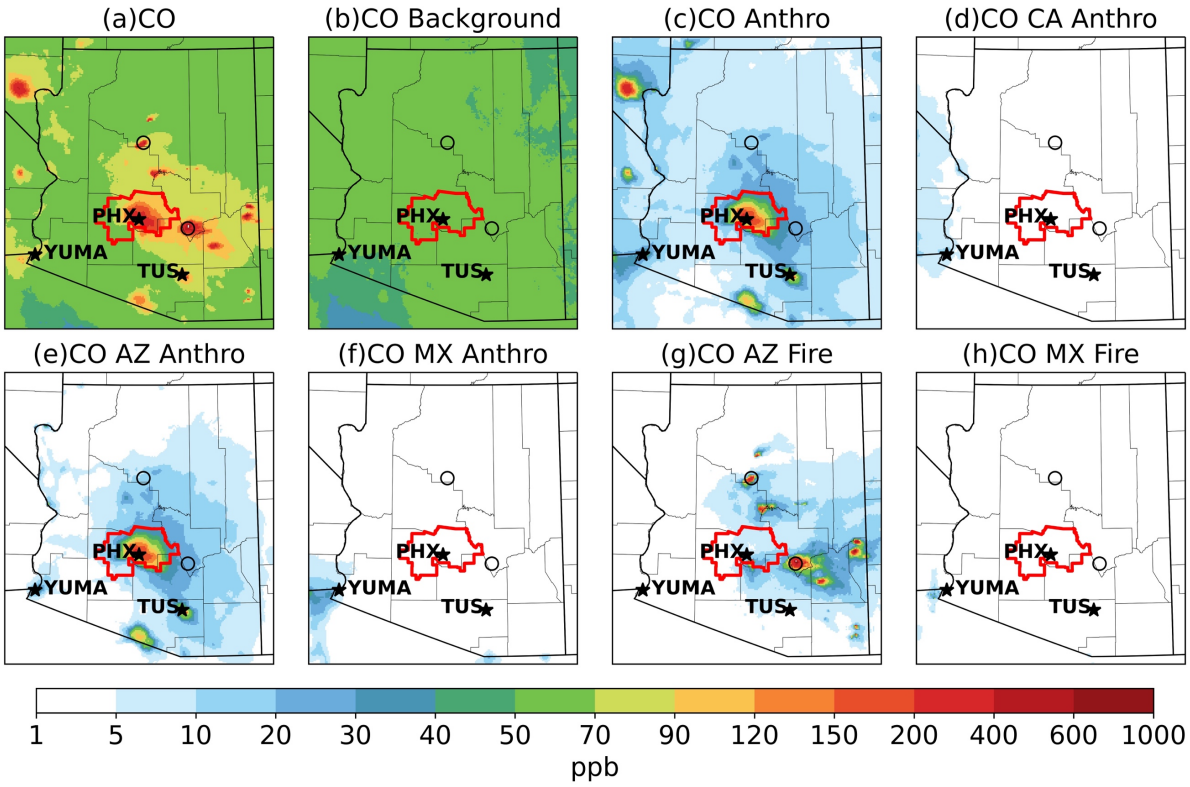

Figure 7. WRF-Chem simulated 90th percentile of surface CO concentrations during June 2021 for total CO (a), and the contributions from different CO sources (b-h). Each panel represents different aspects of CO: (a) total CO, (b) background CO, (c) anthropogenic CO sources, (d) CO from California anthropogenic sources, (e) CO from Arizona anthropogenic sources, (f) CO from Mexico anthropogenic sources, (g) CO from Arizona wildfires, and (h) CO from Mexico wildfires. Key locations such as Phoenix (PHX), Tucson (TUS), and Yuma are marked as stars on the maps. Telegraph and Rafael fires are denoted as unfilled circles.

The "background" CO levels (Figure 7b) are generally constant, ranging between 50 and 70 ppb across the region, which is closely related to international or long-range transport as well as global secondary CO formation. When examining anthropogenic sources, contributions are tagged separately for California (Figure 7d), Arizona (Figure 7e), and Mexico (Figure 7f). The dominant contributions are seen around Arizona's urban areas, particularly Phoenix and Tucson, highlighting the impact of local urban emissions. CO from Mexico also influences southwestern boundaries with Arizona, particularly the city of Yuma, with an estimate of 30 ppb. Contributions from California (Figure 7d) are limited to the state boundaries, with only minor impacts to surface CO (~5 ppb) during this period. As shown in Figure 7g, wildfires in Arizona notably elevate CO levels, especially in areas downwind of active fires with six major wildfire activities identified.

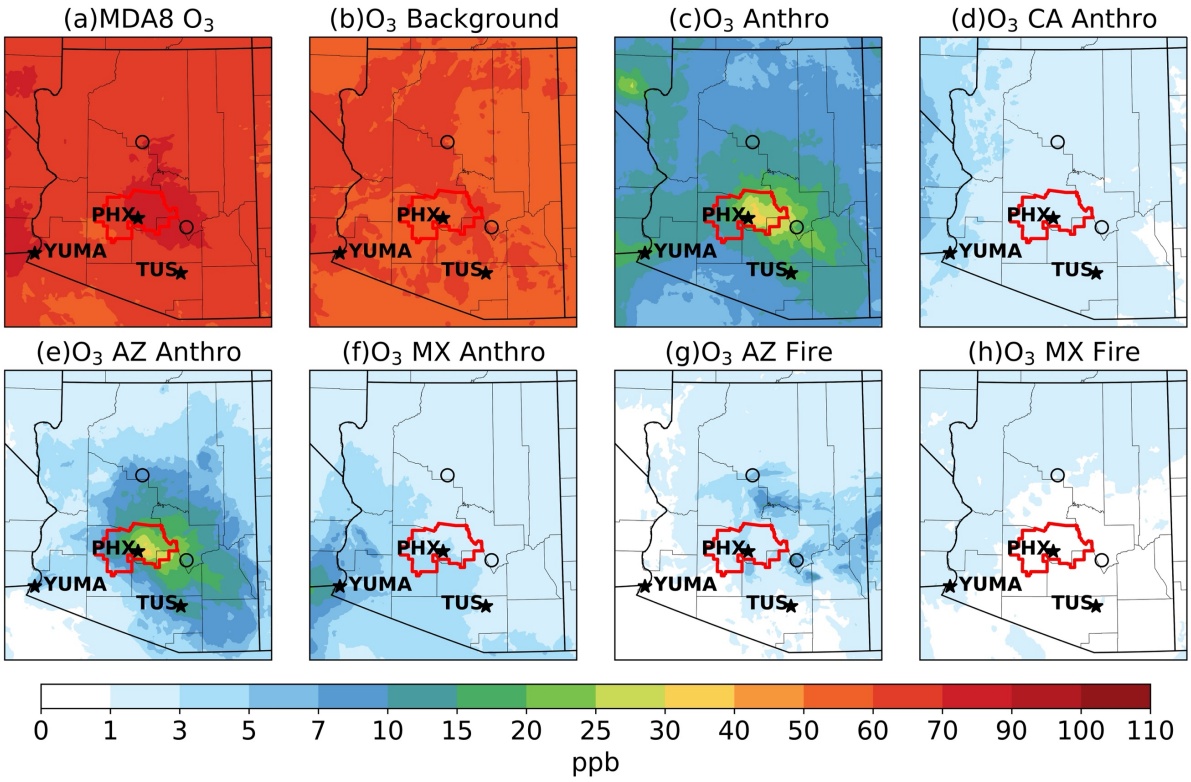

Figure 8. WRF-Chem simulated 90th percentile of O_3 concentrations during June 2021 for (a) MDA8 O_3, and contributions from different sources as (b) background O_3, (c) O_3 from anthropogenic sources, (d) O_3 from California anthropogenic sources, (e) O_3 from Arizona anthropogenic sources, (f) O_3 from Mexico anthropogenic sources, (g) O_3 from Arizona wildfires, and (h) O_3 from Mexico wildfires. Key locations such as Phoenix (PHX), Tucson (TUS), and Yuma are marked as stars on the maps. Telegraph and Rafael fires are denoted as unfilled circles.

Additionally, we examined MDA8 O_3 using the tags, as presented in Figure 8. Note that Figure 8 represents 90th percentile MDA8 O_3 and its corresponding contributions during the month of June rather than instantaneous O_3 concentrations. We see that the MDA8 O_3 concentrations are predominantly high across the region, with the highest levels observed around Phoenix. Figure 8b indicates that the background O_3 levels are uniformly high, approximately 50 ppb, suggesting that even in the absence of local sources, O_3 concentrations remain elevated due to regional and global influences on a monthly basis.

We show in Figures 8c to 8f a regional decomposition of the anthropogenic contributions to O_3 levels. Figure 8c represents all anthropogenic sources, revealing significant contributions, especially around urban centers like Phoenix and Tucson. Figure 8d shows the small impact of

California's anthropogenic emissions on Arizona's O_3 levels during this period only reaching ~3 ppb in Yuma. In contrast, Arizona's anthropogenic contributions to Arizona's O_3 levels (Figure 8e) are substantial (as expected), ranging from 25 to 30 ppb within the nonattainment area. Mexico's anthropogenic contributions (Figure 8f) have a larger impact to O_3 than they do for CO (Figure 7f) in terms of spatial coverage, affecting most of the southern Arizona regions and even reaching Phoenix at 3 ppb. The magnitude is also higher, reaching 10 ppb for Yuma.

Similar to CO, Figures 8g and 8h focus on O_3 contributions from wildfires in Arizona and Mexico, respectively. However, while CO is directly emitted from wildfires, O_3 is chemically formed from precursors such as VOCs and NO_x transported with the smoke. Consequently, the patterns of O_3 differ from those of CO. O_3 can have a larger impact due to the transport of these precursors, leading to significant O_3 formation even far from the wildfire sources. Figure 8g shows that wildfires in Arizona contribute notably to O_3 levels, particularly in areas close to and downwind of the fires. O_3 concentrations range from 1 to 10 ppb, with the highest levels observed near the wildfire locations. The influence of these wildfires extends towards the east and southeast, consistent with the prevailing winds being eastward, and indicating the transport of O_3 precursors and subsequent formation of O_3 in these areas.

Figure 8h highlights the influence of wildfires in Mexico on O_3 levels in Arizona, particularly affecting the southern and southwestern parts of the state. The contributions from Mexico wildfires are less than 3 ppb. The transport of smoke and O_3 precursors from Mexico affects a broader area than CO, reaching as far as Phoenix and diminishing farther north. This underscores the effect of cross-border wildfire emissions on O_3 levels and air quality in southern Arizona, particularly in border regions like Yuma.

We can see in Figures 7 and 8 that Yuma, which is located at the boundaries of Mexico and California, are influenced by local, regional, and transboundary CO and O_3. In Figure 9, we present the modeled and observed hourly O_3 concentrations at local time from Yuma monitoring site (AQS site number: 04-027-8011) for the period between June 14 and June 19, highlighting the contributions from various sources. Two episodes of hourly surface O_3 exceeding 70 ppb are observed on June 15 and June 17, which the WRF-Chem model generally captures, although some discrepancies exist.

The shaded areas reveal the contributions from different sources: background O_3, local and regional anthropogenic emissions, and wildfire emissions from Arizona and Mexico. Figure 9 shows that O_3 levels in Yuma are largely dominated by the background level, primarily from long-range transport and natural sources. However, exceedances of the NAAQS 70 ppb O_3 standard in Yuma are often significantly influenced by emissions from Mexico, even though these contributions are modest in absolute terms. While not dominant overall, these transboundary emissions play a substantial role in elevating O_3 above background levels and contribute to exceedances, particularly on days like June 15, when contributions from Mexico exceed those from Arizona.

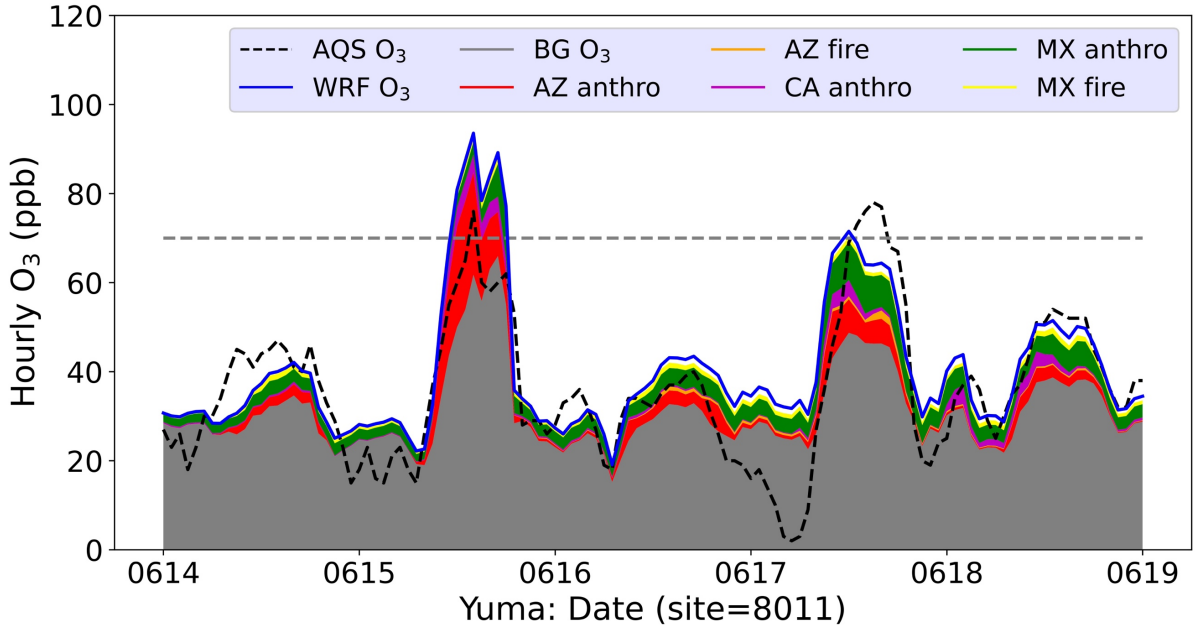

Figure 9. Hourly O_3 concentrations (in ppb) at the Yuma monitoring site (site number: 04-027-8011) between 14-19 June 2021, at local time. The dashed black line represents observed O_3 levels from the AQS, while the solid blue line shows WRF-Chem simulated O_3 concentrations. Shaded areas indicate contributions from various sources: background O_3 (gray), Arizona wildfires (orange), anthropogenic emissions from Mexico (green), anthropogenic emissions from Arizona (red), anthropogenic emissions from California (purple), and Mexico wildfires (yellow).

Figures 7-9 demonstrate the complex interplay of local, regional, and transboundary sources in determining CO and O_3 levels. By examining the contributions of local anthropogenic emissions, wildfire emissions, and regional influences from neighboring states and countries, as well as background levels, these figures provide new perspectives of air quality in the region.

3.2.2 Smoky day O_3 analysis

Fire Contributions to Phoenix O_3. The detailed analysis presented in Section 3.2.1 provides an overview of the key sources of pollution during a fire season in June. In this section, we examine the impact of wildfire smoke plumes on urban areas by examining two specific smoky days (two cases) with a focus on the Phoenix metropolitan area, where the cases are described in Section 3.1. To assess the effects of fire emissions on O_3 concentrations, we conducted an additional set of WRF-Chem simulations without fire emissions for the same period. The simulations without fire emissions serve as a model sensitivity test to evaluate the impact of wildfires.

Figure 10 illustrates the impact of fire emissions on the MDA8 O_3 concentrations for the two cases. The top panels represent Case I for June 15 (a) without fire emissions and (b) with fire emissions. Similarly, the bottom panels depict Case II for June 26 (c) without fire emissions and (d) with fire emissions. The comparison between the left and right panels highlights the significant contribution of wildfire emissions to O_3 levels in the Phoenix metropolitan area.

In Case I (June 15), the presence of fire emissions (Figure 10b) leads to a substantial increase in MDA8 O_3 concentrations, exceeding 110 ppb in areas directly affected by the wildfire plumes. This is in stark contrast to the scenario without fire emissions (panel a), where O_3 levels remain below 90 ppb. The path of the elevated MDA8 O_3 in Figure 10(b) aligns with the HMS smoke coverage depicted in Figure 3.

For Case II (June 26), a similar pattern is observed, albeit with a much weaker intensity. The inclusion of fire emissions (Figure 10d) also results in elevated MDA8 O_3, with peak values reaching around 90 ppb, while without fire emissions (Figure 10c), O_3 levels are significantly lower, generally below 70 ppb. The spatial distribution of MDA8 O_3 also aligns with the mean transport pathway of the wildfire plumes.

The AQS observations, indicated by the colored circles, are generally consistent with the model results when fire emissions are included, demonstrating the model's ability in capturing the impact of wildfire emissions on ground-level O_3 concentrations. The mean bias between model without fire emissions and observations is -7.9 ppb for case I and 9.7 ppb for case II. When fire emissions are included, the mean bias is reduced to -1.8 ppb and 2.9 ppb for the two cases, respectively.

Overall, the sensitivity simulation suggests that wildfires exacerbate O_3 pollution, especially when fire smoke passes through urban areas when photolysis is high. Additionally, it enables us to evaluate the O_3 fire tags. Ideally, the difference in O_3 concentrations when fire emissions are excluded should match the O_3 fire tags. However, studies have shown that this is not always the case mainly due to non-linearity of O_3 chemistry to precursor emissions as well as the spatiotemporal heterogeneity of O_3 chemical regime. The differences between attributing source contributions through sensitivity or tagging approaches have been noted by several studies (e.g., Grewe et al., 2010; Grewe, 2013; Kwok et al., 2015, Mertens et al., 2021, Maruhashi et al., 2024). These studies reported that the sensitivity method could potentially induce large errors (factor of 2), which depend on the degree of linearity of the chemical system. To better understand our tagging approach, we show in Figure 11 the WRF-Chem simulated daytime (7:00-19:00 LT) average of O_3 concentrations for two different cases: Case I on 15 June 2021 (top panels) and Case II on 26 June 2021 (bottom panels). The left panels display the differences in O_3 levels between scenarios with and without fire emissions. The right panels show the daytime average O_3 concentrations attributed to fire emissions (fire tag). The spatial variations observed in the two methods are evidently similar across both cases. However, the values differ by a factor of 1.4, as indicated by the color bar scales, which aligns with previous expectations. Apart from the difference in O_3 magnitude, sensitivity test also shows negative O_3 differences (left panels), which are caused by nonlinear chemical processes. The tagging method does not capture these negative values because the model may not fully represent the O_3 loss processes, such as O_3 titration or the competition between O_3 production and destruction pathways.

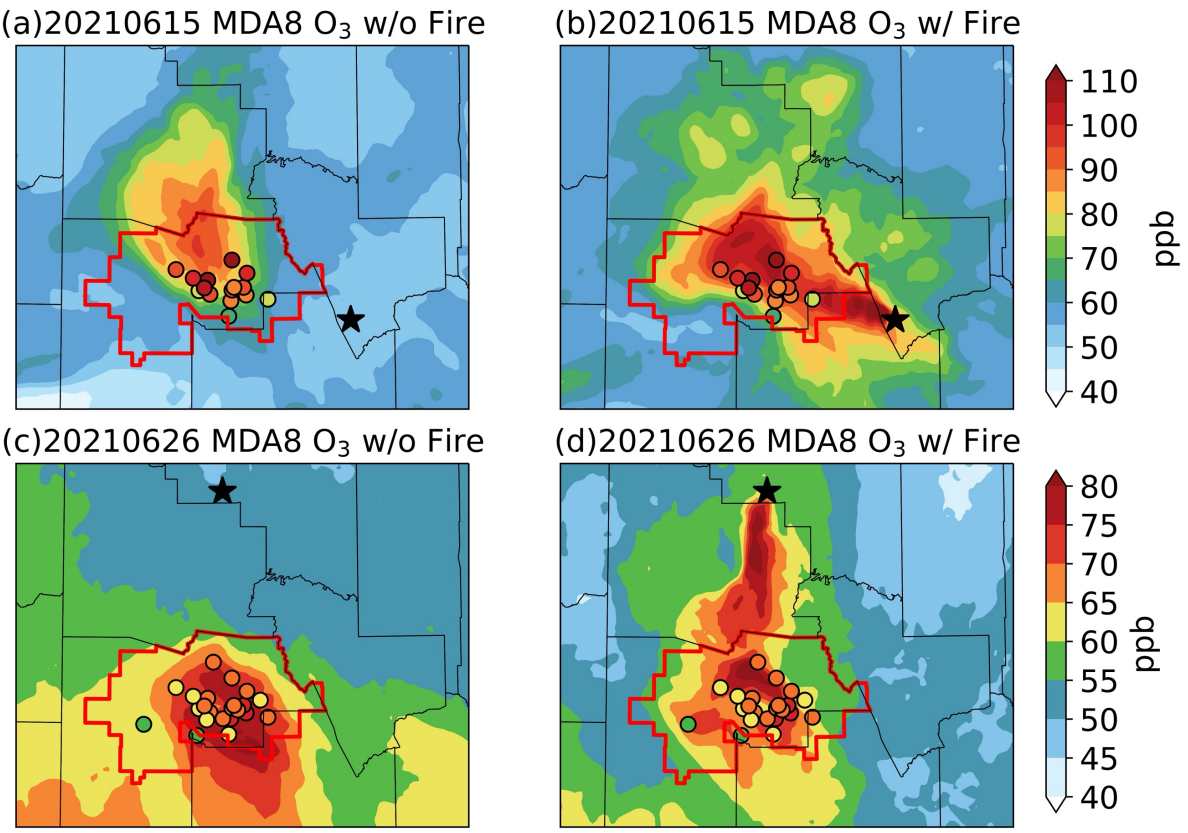

Figure 10. WRF-Chem simulated MDA8 O_3 concentrations for Case I (15 June 2021, top panels) and Case II (26 June 2021, bottom panels) under two conditions: without fire emissions (left panels) and with fire emissions (right panels). AQS observations are represented by colored circles, excluding sites with missing or low-quality data. Stars indicate the locations of the wildfires (top: Telegraph; bottom: Rafael). The red outline represents the designated nonattainment area.

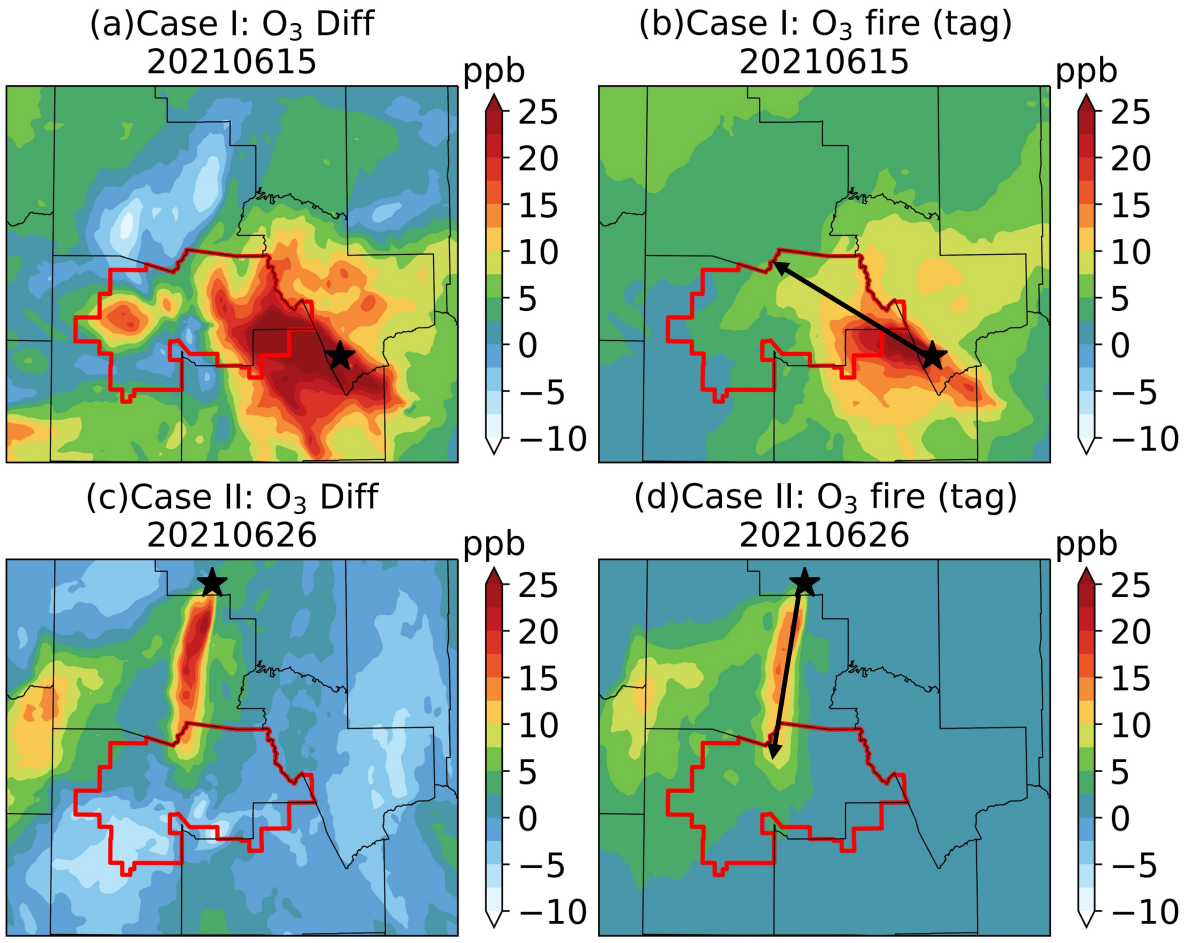

Figure 11. Daytime (7:00-19:00 LT) average O_3 concentrations simulated by WRF-Chem for Case I (15 June 2021, top panels) and Case II (26 June 2021, bottom panels). The left panels show the difference between scenarios with and without fire emissions, while the right panels depict the daytime average O_3 fire tag. Stars mark the wildfire locations (Telegraph Fire at the top and Rafael Fire at the bottom). The red outline denotes the designated nonattainment area. Note that the color bar scales for left and right panels are different. The black arrows indicate the path of smoke plumes.

In addition to examining the spatial variations of O_3 concentrations, we also present the temporal variations of surface hourly O_3 within the Phoenix area in Figure 12, which includes a detailed look at each individual AQS site and the contribution of each O_3 tag to the overall O_3 levels. First, a site located under the plume path with significant O_3 elevation from smoke is selected for each case. Next, a timestamp is chosen when the O_3 fire tag is at its peak to review and compare observations from all AQS sites. The top panels of Figure 14 show the hourly O_3 concentrations

at AQS sites 7024 and 1010 for Case I and Case II, respectively. The locations and site numbers are detailed in Figure 1 and Table S1. For Case I between June 15 and 17, the peak hourly O_3 concentration reached approximately 115 ppb on June 15 at 17:00 local time, aligning with AQS measurements. The contribution from Arizona fire emissions is evident, as indicated by the orange segments in the stacked area chart (Figure 14a). Background O_3 levels (gray shading) constitute the largest portion of the total O_3, accounting for approximately 50%. Local anthropogenic emissions are the next significant contributor, varying between 24% and 40%, depending on the urban setting of the site. A closer examination of other sites during the O_3 peak hour on June 15 reveals that fire contributed O_3 is significant across the area, with values around 15 ppb or 15% (Figure 14b). This indicates that the wildfire events during this period had a substantial impact on elevating O_3 levels.

For Case II, O_3 levels are much lower, peaking at about 80 ppb on June 26 at 11:00. Compared to Case I (Figure 14a), the impact of fires on O_3 levels is less pronounced. After June 26, O_3 levels returned to non-smoky day patterns, with most contributions from local anthropogenic emissions. Figure 14d further illustrates the distribution of O_3 sources across multiple sites at 14:00 on June 26, showing fire contributions of 5-10 ppb or approximately 10%. The background O_3 levels remain consistent with Case I. The differences between these two cases may be attributed to varying meteorological conditions, fire intensity, and/or the spatial distribution of emissions during the two periods. During Case I, Arizona experienced excessive heat and record high temperatures (Figure 2), and the Telegraph Fire had a larger and longer smoke impact than the Rafael Fire in Case II. Unlike Yuma, as shown in Figure 9, O_3 levels in Phoenix are primarily influenced by local emissions, with much smaller contributions from California or Mexico, even with significant contributions from wildfire smoke.

An additional figure comparing the effects of anthropogenic and fire-related emissions on O_3 levels for Case I is provided in Figure S5. This figure shows a pronounced diurnal cycle, with O_3 levels increasing from early morning, peaking around noon to early afternoon (12 to 1pm), and then declining towards the evening. Our results show significant differences between these two emission sources across three urban settings: suburban, urban, and rural. In the early morning and early afternoon, O_3 levels are predominantly influenced by anthropogenic emissions at most AQS sites. However, in the late afternoon, when a fire smoke plume passed through the Phoenix urban

area, the contribution of fire related O_3 increases significantly and, in some rural sites, even surpasses local anthropogenic production.

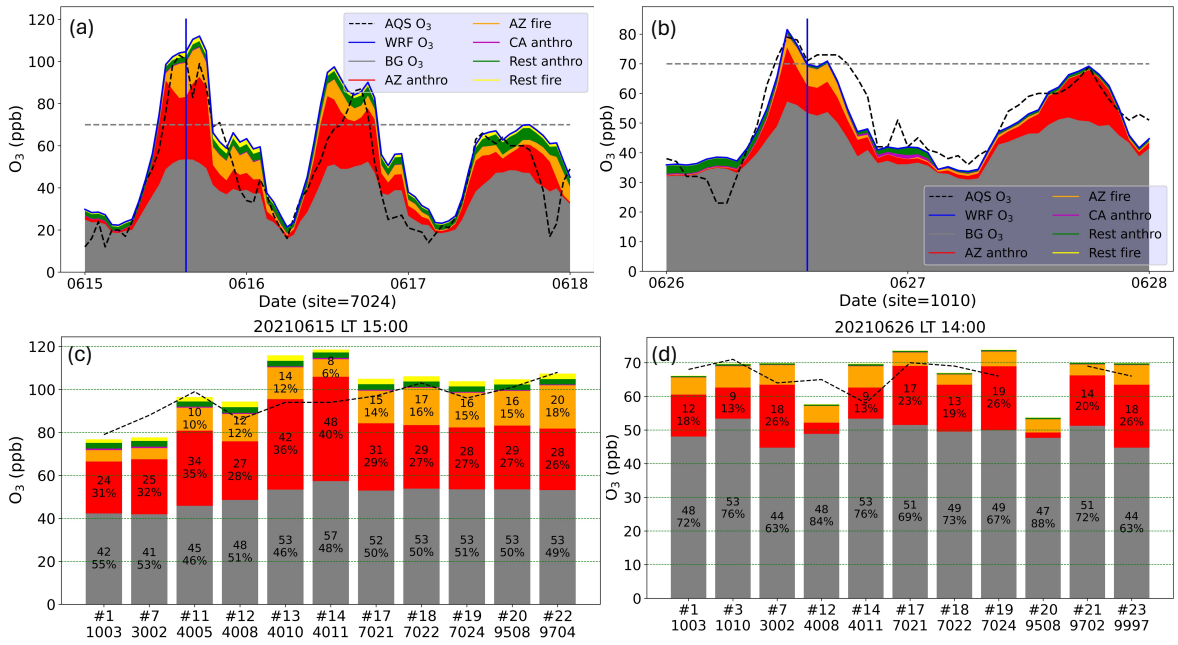

Figure 12. Contribution of each tagged O_3 source to the hourly O_3 concentrations (ppb) for Case I (a-b) and Case II (c-d). The top panels (a, c) show the hourly variations in O_3 concentrations at a single AQS site (#7024 for Case I and #1010 for Case II) from 15-18 June 2021 and 26-28 June 2021, respectively. The bottom panels (b, d) display the contributions of different O_3 sources at multiple sites at the time stamps indicated by the blue vertical lines in (a) and (c). O_3 sources include background O_3 (BG O_3), Arizona anthropogenic (AZ anthro), California anthropogenic (CA anthro), rest of the anthropogenic (Rest anthro), Arizona fire (AZ fire), and rest of the fire (Rest fire).

We also present in Figure 13 the WRF-Chem simulated surface CO concentrations on 15 June 2021 (Case I). By comparing the difference in CO concentrations with fire emissions (Figure 13b) and without fire emissions (Figure 13a) to the CO fire tag (Figure 13d), we observe a similar spatial pattern to that of O_3 in Figure 12. However, the CO fire tag indicates a more extensive area of low CO concentration coverage compared to the sensitivity method. The negative CO values observed in the sensitivity test (panel c) differ from the negative O_3 values, which are primarily driven by nonlinear photochemical processes. Instead, negative CO values likely result from spatial and temporal variations in the CO plume caused by atmospheric transport and mixing. Specifically,

shifts in plume location due to wind patterns and turbulent mixing can create regions where the modeled fire-related CO contributions are lower than the surrounding background levels, leading to apparent negative values.

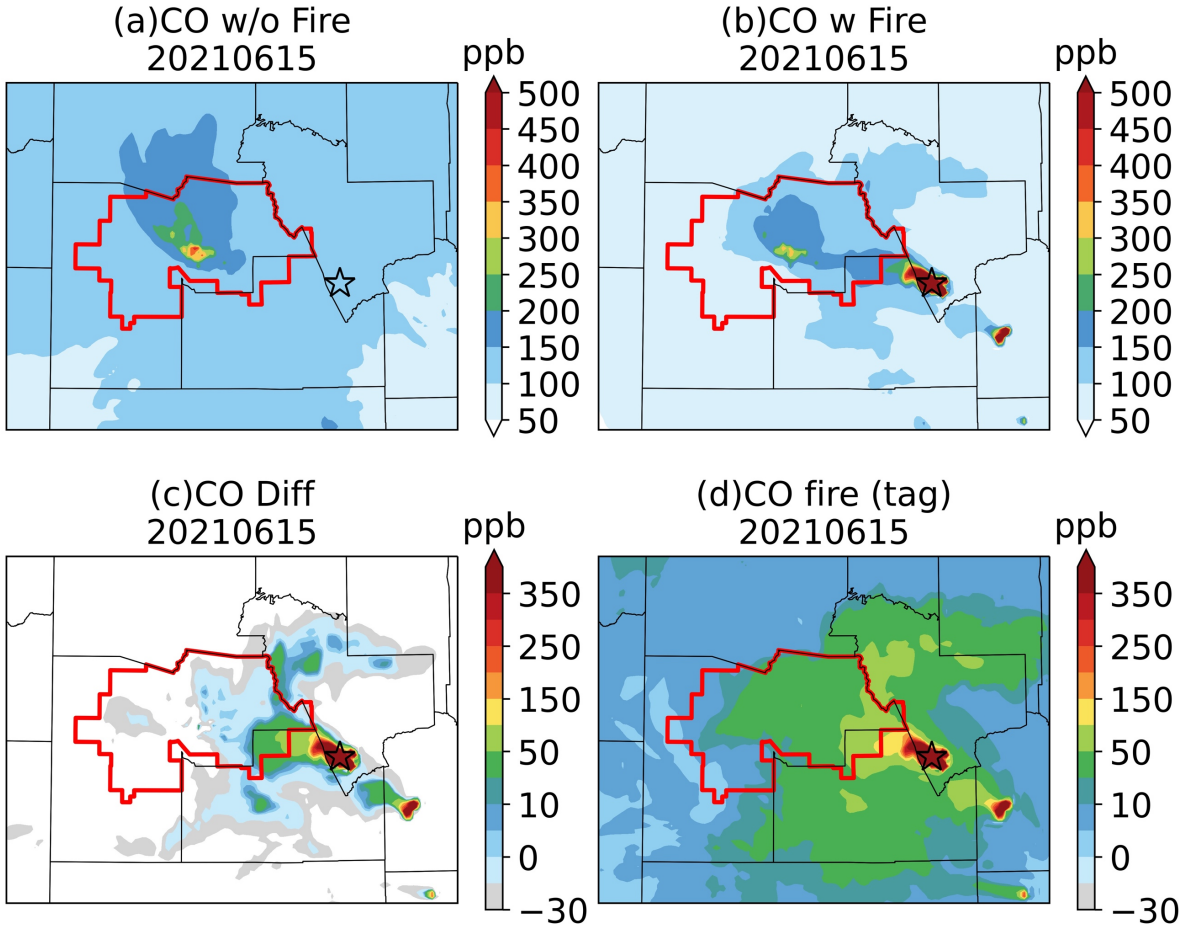

Figure 13. Daytime (7:00-19:00 LT) average surface CO concentrations simulated by WRF-Chem during Case I (15 June 2021) for (a) without fire emissions, (b) with fire emissions, (c) difference between (b) and (a), and (d) CO fire tags. Stars mark the wildfire locations (Telegraph Fire at the top and Rafael Fire at the bottom). The red outline denotes the designated nonattainment area.

Impact of Fire on Chemistry and Meteorology. We show in Figure 14 the temporal variations in the photolysis rate of NO_2 (J_{NO2}), NO_X ($NO+NO_2$) HO_x ($OH+HO_2$), and O_3 concentrations in metro Phoenix (Site 7024) at local time 16:00 over a seven-day period in June 2021, covering Case I under two conditions: with and without fire emissions. This site (see Figure 1) is situated along the plume coverage downwind of the fire. We also included key meteorological variables (net and outgoing longwave radiation, winds, surface temperature and PBL height) and concentration of

black carbon aerosols (which is a light absorbing particle) to elucidate the direct radiative impact of the fires. In Figure 14(a), the photolysis rates of NO_2 (J_{NO2}) are consistently only slightly higher without fire emissions while NO_X concentrations vary across the week (lower in June 14 but slightly higher in June 15 with fire). HO_X levels vary similarly with NO_X during this fire event, possibly associated with VOCs from fires. This results to O_3 in June 15 at 4pm that is significantly higher in the simulation with fire compared to simulation without fire. The net and outgoing longwave radiation, along with black carbon concentration are also higher with fire. Note that there is a significant wind shift from northward to southward (along with lower wind speed) in June 15 when fire is included (Figure 14d), along resulting in the displacement of O_3 and CO hotspot observed in Figure 10 and Figure 13, respectively. This is consistent with the observed exceedance of O_3 levels on the same day.

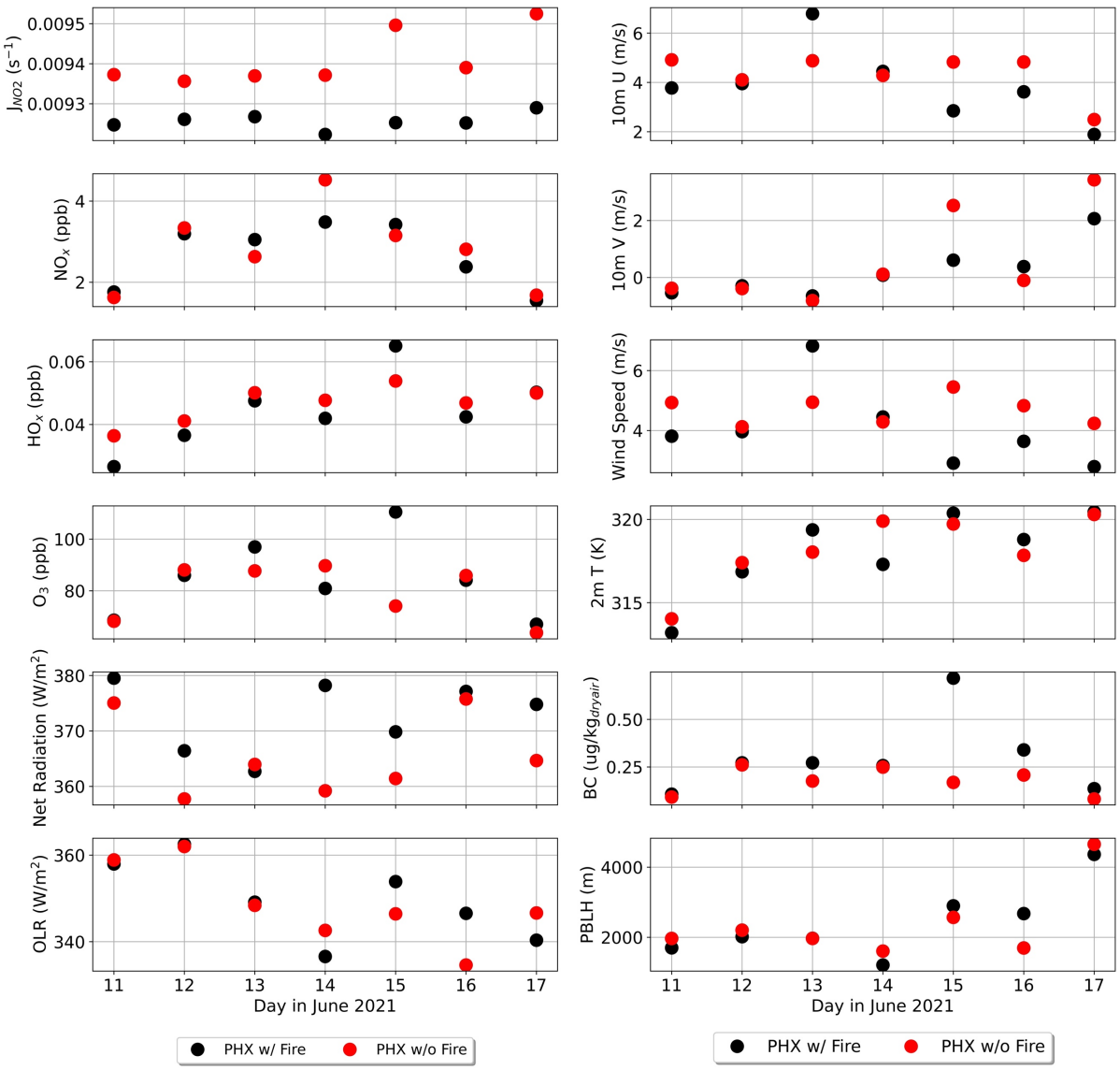

Figure 14. WRF-Chem simulated time series (11-17 June 2021) of daily photolysis rate of NO_2 (J_{NO2}), concentrations of NO_X ($NO+NO_2$; ppb), HO_X ($OH+HO_2$; ppb), and O_3 (ppb), meteorological conditions such as net and outgoing longwave (OLR) radiation (watts/m^2), 10-meter zonal and meridional and zonal wind and wind speed (10m U and V, Wind Speed (m/s), 2-meter air temperature (K), concentration of black carbon (BC) aerosols (µg/m^3), and planetary boundary layer height (PBLH). All these are sampled at 16:00 local time in Phoenix (Site 19 - #7024). The black markers represent the values with fire emissions, while the red markers indicate values without fire emissions.

630

To further investigate the fire impact, we present in Figure 15 a cross-sectional view of the smoke plume as it travels towards Phoenix during Case I, highlighting the concentrations of multiple atmospheric pollutants, including O_3, CO, NO_x, HCHO (formaldehyde), $PM_{2.5}$ (particulate matter), and PAN (peroxyacetyl nitrate). Near the fire location, concentrations of CO, NO_x, HCHO, and $PM_{2.5}$, which are primary pollutants directly emitted from the fire, are high, whereas O_3 concentrations are lower. As the smoke moves closer to the urban region, NO_x levels in the boundary layer increase significantly, along with O_3 levels reaching 100 ppb above the ground. Levels of NO_X from fires diminishes at a faster rate than HCHO and $PM_{2.5}$ levels along the trajectory. It is clear from the figure that pollutants from the fires are transported towards the valley.

This is particularly true for PAN which shows an enhancement above the valley along with CO and $PM_{2.5}$. These enhancements aloft are not present in the cross-section of WRF-Chem simulation without fire emissions (see Supplemental Figure S7). Previous studies have indicated that the rapid conversion of NO_x to PAN can limit O_3 production near fires, especially at low temperatures, but the decomposition of PAN can lead to additional O_3 production further downwind of the fires especially in the presence of higher amounts of VOCs (Alvarado et al., 2010; Jaffe et al., 2013). The concentrations of O_3, CO, NO_x, and PAN from fire tags presented in Figure S6 (alongside Figure S7) further demonstrate that fire smoke exacerbates urban O_3 levels, while the exceedance is predominantly from local production.

In summary, this cross-sectional analysis illustrates the complex vertical and horizontal distribution of various pollutants and their transformations within a smoke plume traveling towards Phoenix. The interaction between primary emissions from fires, secondary pollutants formed during transport, and the presence of local anthropogenic emissions in the urban environment highlights the multifaceted nature of urban air quality impacts during wildfire events.

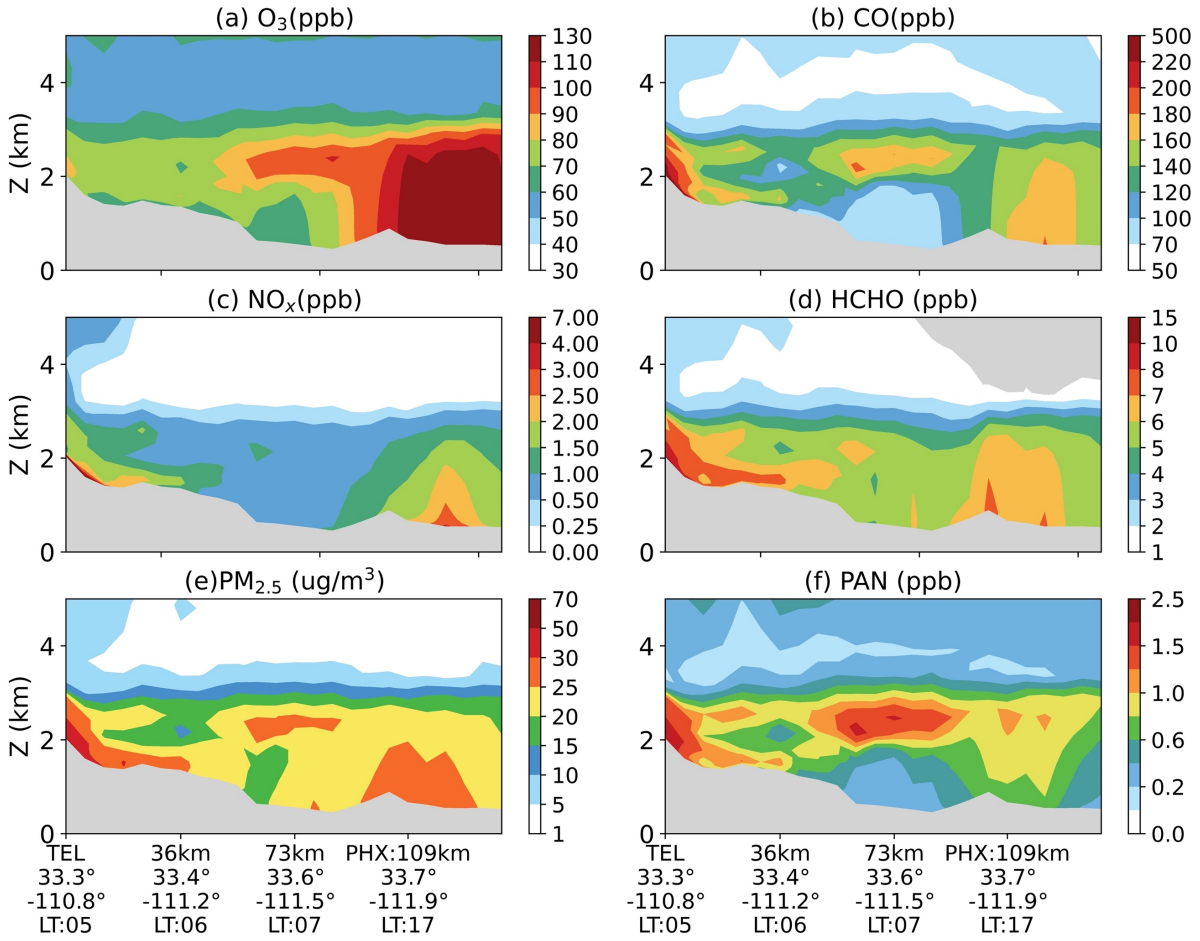

Figure 15. Cross-sectional analysis of a smoke plume traveling towards Phoenix during 15 June 2021, showing vertical and horizontal distribution of various pollutants. The subplots represent concentrations of (a) O_3, (b) CO, (c) NO_x, (d) HCHO, (e) $PM_{2.5}$, and (f) PAN (Peroxyacetyl Nitrate) across different altitudes and distances from the fire where TEL means Telegraph. The plume path is denoted in Figure 11. The gray shading represents the topography heights.

Fire-induced Changes in Chemical Regime. We show in Figure 16 the associated impact of fires on the chemical regimes of O_3 formation over Phoenix at local time 14:00. Here, two key indicators are chosen to illustrate this impact: the $HCHO/NO_2$ ratio, also known as the Formaldehyde to NO_2 Ratio (FNR), and the H_2O_2/HNO_3 ratio (Sillman, 1995; Tonnesen et al., 2000). The $HCHO/NO_2$ ratio (FNR) has been used in previous studies as an indicator for determining the sensitivity of O_3 formation to either VOCs or NO_x (Martin et al., 2004; Jin et al., 2020; Mirrezaei et al., 2024). A higher FNR indicates a NO_x-limited regime, where O_3 formation is more sensitive to changes in NO_x emissions, while a lower FNR points to a VOC-limited regime, where O_3 formation is more

responsive to changes in VOCs. In the context of wildfire smoke, the influx of VOCs from the fires can shift the chemical regime from VOC-limited to NO_x-limited, altering the dynamics of O_3 production in the urban area. This shift can lead to unexpected increases in O_3 levels as the balance of precursors is altered by the incoming smoke plume. To complement the primary HCHO/NO_2-based classification of chemical regimes, we employed the H_2O_2/HNO_3 ratio as an additional indicator to provide context regarding the oxidizing capacity of the atmosphere and the contributions of various chemical pathways to O_3 production. H_2O_2 (hydrogen peroxide) is a product of VOC oxidation, while HNO_3 (nitric acid) results from the oxidation of NO_x. A higher ratio suggests an environment with abundant VOC oxidation, often associated with high levels of O_3 production (Sillman, 1995). Conversely, a lower ratio indicates a dominance of NO_x oxidation pathways, which can suppress O_3 formation under certain conditions.

However, uncertainties in the threshold values for the H_2O_2/HNO_3 ratio exist across studies. For instance, Sillman (1995) suggested a threshold of 0.4, where values above indicate a NO_x-limited regime, and values below indicate a VOC-limited regime. Subsequently, Sillman et al. (1997) proposed a lower threshold of 0.2, while Lu and Chang (1998) introduced a broader transition range of 0.8–1.2. Zhang et al. (2009) later recommended a higher threshold of 2.4 for summertime conditions. These discrepancies highlight the challenges in applying a universal threshold and emphasize the supplemental nature of this metric in our analysis. In this study, regardless of the specific thresholds used to define VOC-limited or NO_x-limited regimes, we focus on the changes in the H_2O_2/HNO_3 ratio in response to wildfire smoke.

The presence of wildfire emissions can increase the levels of both VOCs and NO_x, thereby influencing this ratio and providing insights into the changing oxidative environment over Phoenix. The relative change in VOCs and NO_x will affect O_3 sensitivity, depending on which of these pollutants has a larger percentage change. Miech et al. (2024) found that at Phoenix JLG supersite, when the sensitivity is under VOC-limited, FNR is higher than normal suggesting elevated VOCs relative to NO_2 under a smoke event and shifting the sensitivity towards a transitional or NO_x-limited. This is also seen in Figure 15 where levels of CO and HCHO are relatively elevated than NO_X along the fire plume trajectory.

In Figure 16, the analysis of these two surface ratios reveals how wildfire smoke alters the chemical regime over Phoenix at local time 14:00 when O_3 production is expected to peak. Without the

smoke plume, the majority of Phoenix urban area in the early afternoon, when the photolysis is highest, is under a transitional/NO_x-limited regime (Figure 16a). With the presence of smoke, additional NO_x and VOCs are brought to the region and the regime shifts towards more NOx-limited in the central urban region, as seen by the increase (orange contours) in the FNR (Figure 16c), consistent with Miech et al. (2024). In contrast, FNR decreases across the broader extent of the fire, (blue contours), most likely with the introduction of NO_X from PAN decomposition further downwind. Accordingly, the H_2O_2/HNO_3 ratio provides a similar picture of the increasing ratios in the metropolitan area due to the influx of emissions from the fires.

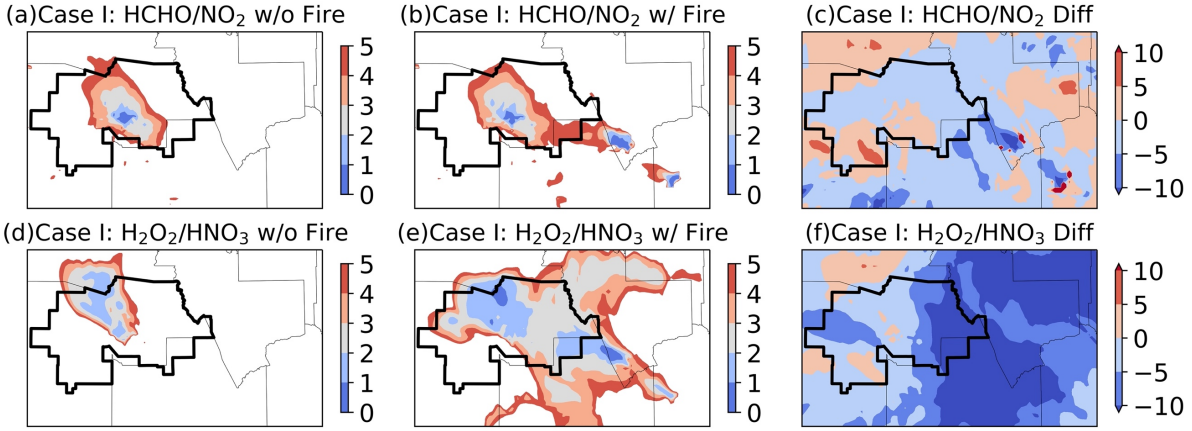

Figure 16. Sensitivity analysis of different ratios in Case I at local time 14:00 under conditions without and with fire. The top row (a-c) is the surface HCHO/NO_2 ratio, while the bottom row (d-f) depicts the surface H_2O_2/HNO_3 ratio. Ratios larger than 5 are shown as white space. (a) and (d) show the respective ratios without fire, and (b) and (e) display the ratios with fire. (c) and (f) represent the differences in these ratios between the scenarios with and without fire. The red color in (c) and (f) indicates a shift towards a more NO_x-limited regime, and blue indicates a shift towards a more VOC-limited regime.

4. Conclusion

This study focuses on the contribution of wildfire emissions on surface O_3 levels in the Phoenix metropolitan area during June 2021, a period characterized by extreme heat and drought conditions. We apply model sensitivity and species tagging approaches in the WRF-Chem model to quantify its contribution relative to other sources. Two specific cases (Telegraph and Rafael fires) are chosen for analyzing the wildfire impact on urban regions. During these cases, the MDA8 O_3 is

observed to exceed the NAAQS standard (70 ppb), especially for case I (Telegraph fire), with concentrations reaching 110 ppb.

Overall, the O_3 levels in Arizona are influenced by a combination of background levels, local anthropogenic emissions, and wildfire contributions. The highest O_3 levels were observed around urban centers, with wildfires significantly contributing to elevated O_3, especially near the fire sites and downwind areas. The spatial and temporal distributions of CO and O_3, as well as the contributions from different tags in Arizona during the wildfire season, reveal significant contributions of both anthropogenic and wildfire emissions to CO levels across the state, with local urban emissions still playing a dominant role in areas like Phoenix and Tucson. However, wildfire emissions were particularly impactful in regions downwind of the fires.

In fact, our simulations show that wildfire emissions notably increased the MDA8 O_3 levels during two fire plume case studies that we examined. The Telegraph Fire, in particular, contributed to significant O_3 levels on June 15. The results demonstrated that background O_3 levels account the bulk of total O_3 (around 50%), with local anthropogenic emissions contributing significantly (24% to 40%) depending on the urban setting. During peak O_3 hours, fire-contributed O_3 was significant across multiple sites, ranging from 5 to 23 ppb or 5% to 21 % of total O_3 levels, with an average of 15 ppb or 15%. Without smoke, the Phoenix urban area is primarily under a transition to NO_x-limited regime in the early afternoon when O_3 photolysis rate is highest. With smoke present, the central urban region becomes more NO_x-limited due to the addition of VOCs transported from the fires relative to NO_x which is already high from local anthropogenic emissions. In contrast, the suburban and rural areas downwind of the fires generally experience a decrease in the ratio shifting towards a more VOC-limited regime, which is likely due to the addition of NO_x from fires as a result of thermal decomposition of PAN from the fires transported to these areas.

By closely investigating these tags, we also find differences between Phoenix and Yuma. Unlike Yuma, where O_3 levels are significantly influenced by transboundary emissions from California and Mexico, Phoenix's O_3 levels are primarily driven by local emissions, with much smaller contributions from these external sources during the study period. Specifically for a smoky day, during the diurnal cycle of O_3 levels, anthropogenic emission contributed local O_3 production dominate in the early morning and early afternoon, while fire-related O_3 contributions increase significantly in the late afternoon when a smoke plume passes through. This pattern is observed

across suburban, urban, and rural settings, with fire related O_3 sometimes surpassing local anthropogenic production in rural areas.

Our study has several limitations. First, we only tagged NO_x emissions, which may not fully capture O_3 dynamics in VOC-limited regions where VOCs play a more significant role in O_3 formation. Additionally, the limited number of cases analyzed reduces the generalizability of the results. Expanding the study to include more cases would improve robustness. Furthermore, the absence of vertical profile data limits the depth of the analysis, particularly for understanding pollutant distributions in the upper atmosphere. In the future, with more spatial coverage, including diurnal variation data from Tropospheric Emissions: Monitoring of Pollution (TEMPO), would enhance the temporal and spatial representation of O_3 and aerosol concentrations. Refinements in fire emission estimates from FINN, plume rise calculations, and the validation of aerosol direct radiative effects on dynamics and thermodynamics, particularly radiation fluxes would increase model accuracy. Lastly, incorporating more detailed sectoral tags would better differentiate emission sources and improve O_3 and aerosol impact assessments. Moreover, since tagged O_3 is represented as tracers in the model, its production and immediate loss are primarily captured, while some loss processes may not be fully accounted for. Processes such as detailed fire-plume shading effects and nighttime O_3 titration chemistry may therefore be underrepresented.

As has been suggested by previous studies, the substantial enhancements in O_3 concentrations due to wildfire emissions highlight the necessity of accounting for wildfire impacts in formulating effective air quality management strategies. Such strategies should consider the influence of fire emissions on urban O_3 and more notably their subsequent interactions with local emissions, chemistry, and meteorology (e.g., He et al., 2024) to help provide additional perspectives on current O_3 pollution assessments. This is especially the case over urban areas in semi-arid/arid environments like southwest United States, where confounding (and compounding) factors arising from meteorological extremes and dynamical challenges due to complex topography are present; notwithstanding the effect of climate change to increasing global aridity and fire frequency and intensity. The adoption of source attribution approaches (including the use of data-driven techniques) within coupled weather-air quality models, accompanied by more comprehensive evaluation, can be a useful complementary activity to consider in helping support current approaches in understanding O_3.

Code and Data Availability Statement.

The WRF-Chem model is publicly available at https://github.com/wrf-model/WRF (last access: 25 June 2022). The model outputs can be provided upon request to the corresponding author. EPA AQS and PAMS hourly and daily datasets are available at https://aqs.epa.gov/aqsweb/airdata/download_files.html.

Author contributions.

YG and AA designed the research. YG performed the model runs and subsequent analysis. YG wrote the paper with contributions from AA and AS. AM helped with the satellite data analysis.

Competing Interests.

Some authors are members of the editorial board of journal Atmospheric Chemistry and Physics.

Acknowledgments.

We especially acknowledge Dr. Gabriele Pfister and Dr. Louisa Emmons at NCAR/ACOM for kindly providing the guidance for implementing tagging in WRF-Chem. We also greatly appreciate the code availability shared with the public through Lupaşcu et al. (2019), which this study was built upon. We also thank Dr. Matthew Pace, Dr. Rene Nsanzineza, and Michael Graves at the Arizona Department of Environmental Quality (ADEQ) for the help with observations for the state of Arizona.

Financial Support.

This work is supported by the Arizona Board of Regents (ABOR) Grant from the Technology and Research Initiative Fund (TRIF).

References:

Abatzoglou, J. T. and Williams, A. P.: Impact of anthropogenic climate change on wildfire across western US forests, Proceedings of the National Academy of Sciences, 113, 11770-11775, doi:10.1073/pnas.1607171113, 2016.

Adhikari, A. and Yin, J.: Short-Term Effects of Ambient Ozone, PM2.5, and Meteorological Factors on COVID-19 Confirmed Cases and Deaths in Queens, New York, International Journal of Environmental Research and Public Health, 17, 4047, doi:10.3390/ijerph17114047, 2020.

Akagi, S. K., Craven, J. S., Taylor, J. W., McMeeking, G. R., Yokelson, R. J., Burling, I. R., Urbanski, S. P., Wold, C. E., Seinfeld, J. H., Coe, H., Alvarado, M. J., and Weise, D. R.: Evolution of trace gases and particles emitted by a chaparral fire in California, Atmos. Chem. Phys., 12, 1397-1421, 10.5194/acp-12-1397-2012, 2012.

Alonso-Blanco, E., Castro, A., Calvo, A. I., Pont, V., Mallet, M., and Fraile, R.: Wildfire smoke plumes transport under a subsidence inversion: Climate and health implications in a distant urban area, Science of The Total Environment, 619-620, 988-1002, https://doi.org/10.1016/j.scitotenv.2017.11.142, 2018.

Andreae, M. O.: Emission of trace gases and aerosols from biomass burning – an updated assessment, Atmos. Chem. Phys., 19, 8523-8546, 10.5194/acp-19-8523-2019, 2019.

Betito, G., Arellano, A., and Sorooshian, A.: Influence of Transboundary Pollution on the Variability of Surface Ozone Concentrations in the Desert Southwest of the U.S.: Case Study for Arizona, Atmosphere, 15, 401, 10.3390/atmos15040401, 2024.

Brey, S. J., Ruminski, M., Atwood, S. A., and Fischer, E. V.: Connecting smoke plumes to sources using Hazard Mapping System (HMS) smoke and fire location data over North America, Atmos. Chem. Phys., 18, 1745–1761, https://doi.org/10.5194/acp-18-1745-2018, 2018.

Burke, M., Childs, M. L., de la Cuesta, B., Qiu, M., Li, J., Gould, C. F., Heft-Neal, S., and Wara, M.: The contribution of wildfire to PM(2.5) trends in the USA, Nature, 622, 761-766, 10.1038/s41586-023-06522-6, 2023.

Butler, T., Lupascu, A., and Nalam, A.: Attribution of ground-level ozone to anthropogenic and natural sources of nitrogen oxides and reactive carbon in a global chemical transport model, Atmos. Chem. Phys., 20, 10707-10731, 10.5194/acp-20-10707-2020, 2020.

Butler, T., Lupascu, A., Coates, J., and Zhu, S.: TOAST 1.0: Tropospheric Ozone Attribution of Sources with Tagging for CESM 1.2.2, Geosci. Model Dev., 11, 2825-2840, 10.5194/gmd-11-2825-2018, 2018.

Buysse, C. E., Kaulfus, A., Nair, U., and Jaffe, D. A.: Relationships between Particulate Matter, Ozone, and Nitrogen Oxides during Urban Smoke Events in the Western US, Environmental Science & Technology, 53, 12519-12528, 10.1021/acs.est.9b05241, 2019.

Cazorla, M., Herrera, E.: An ozonesonde evaluation of spaceborne observations in the Andean tropics. *Scitific Report,* 12, 15942, https://doi.org/10.1038/s41598-022-20303-7, 2022.

Clappier, A., Belis, C. A., Pernigotti, D., and Thunis, P.: Source apportionment and sensitivity analysis: two methodologies with two different purposes, Geosci. Model Dev., 10, 4245–4256, https://doi.org/10.5194/gmd-10-4245-2017, 2017.

Cohan, D. S., Hakami, A., Hu, Y., and Russell, A. G.: Nonlinear Response of Ozone to Emissions: Source Apportionment and Sensitivity Analysis, Environmental Science & Technology, 39, 6739-6748, 10.1021/es048664m, 2005.

Collet, S., Minoura, H., Kidokoro, T., Sonoda, Y., Kinugasa, Y., Karamchandani, P., Johnson, J., Shah, T., Jung, J., and DenBleyker, A.: Future year ozone source attribution modeling studies for the eastern and western United States, Journal of the Air & Waste Management Association, 64, 1174-1185, 10.1080/10962247.2014.936629, 2014.

Conservation Biology Institute: Potential Natural Vegetation Type Dataset, Data Basin, https://databasin.org/maps/new/#datasets=43a107f2f0c048f8a87a97adf0368ee9 (last access: 9 November 2024), 2024.

Copernicus Sentinel data processed by ESA, German Aerospace Center (DLR): Sentinel-5P TROPOMI Total Ozone Column 1-Orbit L2 5.5km x 3.5km, Greenbelt, MD, USA, Goddard Earth Sciences Data and Information Services Center (GES DISC), Accessed: 17 November 2024., 10.5270/S5P-ft13p57, 2020.

Copernicus Sentinel data processed by ESA, German Aerospace Center-Institute for Environmental Research/University of Bremen (DLR_IUP): Sentinel-5P TROPOMI Tropospheric Ozone Column, Greenbelt, MD, USA, Goddard Earth Sciences Data and Information Services Center (GES DISC), Accessed: 17 November 2024., 10.5270/S5P-hcp1l2m, 2020.

De la Paz, D., Borge, R., de Andrés, J. M., Tovar, L., Sarwar, G., and Napelenok, S. L.: Summertime tropospheric ozone source apportionment study in the Madrid region (Spain), Atmos. Chem. Phys., 24, 4949-4972, 10.5194/acp-24-4949-2024, 2024.

Demerjian, K. L.: A review of national monitoring networks in North America, Atmospheric Environment, 34, 1861-1884, https://doi.org/10.1016/S1352-2310(99)00452-5, 2000.

Duncan, B. N., Yoshida, Y., Olson, J. R., Sillman, S., Martin, R. V., Lamsal, L., Hu, Y., Pickering, K. E., Retscher, C., Allen, D. J., and Crawford, J. H.: Application of OMI observations to a space-based indicator of NOx and VOC controls on surface ozone formation, Atmos. Environ., 44, 2213–2223, https://doi.org/10.1016/j.atmosenv.2010.03.010, 2010.

Emmons, L. K., Hess, P. G., Lamarque, J. F., and Pfister, G. G.: Tagged ozone mechanism for MOZART-4, CAM-chem and other chemical transport models, Geosci. Model Dev., 5, 1531-1542, 10.5194/gmd-5-1531-2012, 2012.

Freitas, S. R., Longo, K. M., Chatfield, R., Latham, D., Silva Dias, M. A. F., Andreae, M. O., Prins, E., Santos, J. C., Gielow, R., and Carvalho Jr, J. A.: Including the sub-grid scale plume rise of vegetation fires in low resolution atmospheric transport models, Atmos. Chem. Phys., 7, 3385-3398, 10.5194/acp-7-3385-2007, 2007.

Gard, H. and Garrett, M.: Wildfire smoke stopped Phoenix from breaking record high of 115 degrees, CNN Weather, 2021.

Goldberg, D. L., Vinciguerra, T. P., Anderson, D. C., Hembeck, L., Canty, T. P., Ehrman, S. H., Dickerson, R. R.: CAMx ozone source attribution in the eastern United States using guidance from observations during DISCOVER-AQ Maryland. Geophysical research letters, 43(5), 2249-2258, doi:10.1002/2015GL067332, 2016.

Greenslade, M., Guo, Y., Betito, G., Mirrezaei, M. A., Roychoudhury, C., Arellano, A. F., and Sorooshian, A.: On ozone's weekly cycle for different seasons in Arizona, Atmospheric Environment, 334, 120703, https://doi.org/10.1016/j.atmosenv.2024.120703, 2024.

Grell, G. A., Peckham, S. E., Schmitz, R., McKeen, S. A., Frost, G., Skamarock, W. C., and Eder, B.: Fully coupled "online" chemistry within the WRF model, Atmospheric Environment, 39, 6957-6975, https://doi.org/10.1016/j.atmosenv.2005.04.027, 2005.

Grewe, V., Tsati, E., and Hoor, P.: On the attribution of contributions of atmospheric trace gases to emissions in atmospheric model applications, Geosci. Model Dev., 3, 487-499, 10.5194/gmd-3-487-2010, 2010.

Grewe, V., Dahlmann, K., Matthes, S., and Steinbrecht, W.: Attributing ozone to NOx emissions: Implications for climate mitigation measures, Atmospheric Environment, 59, 102-107, https://doi.org/10.1016/j.atmosenv.2012.05.002, 2012.

Grewe, V.: A generalized tagging method, Geosci. Model Dev., 6, 247–253, https://doi.org/10.5194/gmd-6-247-2013, 2013.

Grewe, V., Tsati, E., Mertens, M., Frömming, C., and Jöckel, P.: Contribution of emissions to concentrations: the TAGGING 1.0 submodel based on the Modular Earth Submodel System (MESSy 2.52), Geosci. Model Dev., 10, 2615-2633, 10.5194/gmd-10-2615-2017, 2017.

Guenther, A.: Estimates of global terrestrial isoprene emissions using MEGAN (Model of Emissions of Gases and Aerosols from Nature), Atmospheric Chemistry and Physics, 7, 4327-4327, 10.5194/acp-6-3181-2006, 2007.

Guenther, A., Karl, T., Harley, P., Wiedinmyer, C., Palmer, P. I., and Geron, C.: Estimates of global terrestrial isoprene emissions using MEGAN (Model of Emissions of Gases and Aerosols from Nature), Atmos. Chem. Phys., 6, 3181-3210, 10.5194/acp-6-3181-2006, 2006.

Gao, J., Zhu, B., Xiao, H., Kang, H., Hou, X., & Shao, P., A case study of surface ozone source apportionment during a high concentration episode, under frequent shifting wind conditions over the Yangtze River Delta, China. *Science of the Total Environment*, *544*, 853-863, 10.1016/j.scitotenv.2015.12.039, 2016

Guo, Y., Roychoudhury, C., Mirrezaei, M. A., Kumar, R., Sorooshian, A., and Arellano, A. F.: Investigating ground-level ozone pollution in semi-arid and arid regions of Arizona using WRF-Chem v4.4 modeling, Geosci. Model Dev., 17, 4331-4353, 10.5194/gmd-17-4331-2024, 2024.

Hakami, A., Seinfeld, J. H., Chai, T., Tang, Y., Carmichael, G. R., & Sandu, A., Adjoint sensitivity analysis of ozone nonattainment over the continental United States. Environmental science & technology, 40(12), 3855-3864, 10.1021/es052135g, 2006.

Hakami, A., Henze, D. K., Seinfeld, J. H., Singh, K., Sandu, A., Kim, S., Li, Q., The adjoint of CMAQ. Environmental science & technology, 41(22), 7807-7817, 10.1021/es070944p, 2007.

He C., Kumar R., Tang, W., Pfister, G., Xu, Y., Qian. Y., Brasseur, G., Air Pollution Interactions with Weather and Climate Extremes: Current Knowledge, Gaps, and Future Directions. Current Pollution Reports, 22, 1-3, 10.1007/s40726-024-00296-9, 2024.

Huangfu, P. and Atkinson, R.: Long-term exposure to NO2 and O3 and all-cause and respiratory mortality: A systematic review and meta-analysis, Environment International, 144, 105998, https://doi.org/10.1016/j.envint.2020.105998, 2020.

Heue, K.-P., Eichmann, K.-U. & Valks, P.: TROPOMI/S5P ATBD of Tropospheric Ozone Data Products. https://sentinels.copernicus.eu/documents/247904/2476257/Sentinel-5P-ATBD-TROPOMI-Tropospheric-Ozone.pdf/d2106102-b5c3-4d28-b752-026e3448aab2?t=1625507455328. Accessed 17 November 2024, 2021.

Jaffe, D. A. and Wigder, N. L.: Ozone production from wildfires: A critical review, Atmospheric Environment, 51, 1-10, https://doi.org/10.1016/j.atmosenv.2011.11.063, 2012.

Jaffe, D. A., Wigder, N., Downey, N., Pfister, G., Boynard, A., and Reid, S. B.: Impact of Wildfires on Ozone Exceptional Events in the Western U.S, Environmental Science & Technology, 47, 11065-11072, 10.1021/es402164f, 2013.

Jaffe, D. A., O'Neill, S. M., Larkin, N. K., Holder, A. L., Peterson, D. L., Halofsky, J. E., and Rappold, A. G.: Wildfire and prescribed burning impacts on air quality in the United States, Journal of the Air & Waste Management Association, 70, 583-615, 10.1080/10962247.2020.1749731, 2020.

Jin, X., Fiore, A., Boersma, K. F., Smedt, I. D., & Valin, L., Inferring changes in summertime surface Ozone–NO x–VOC chemistry over US urban areas from two decades of satellite and ground-based observations, Environmental science & technology, 54(11), 6518-6529, doi: 10.1021/acs.est.9b07785, 2020

Jin, X., Fiore, A. M., and Cohen, R. C.: Space-Based Observations of Ozone Precursors within California Wildfire Plumes and the Impacts on Ozone-NOx-VOC Chemistry, Environmental Science & Technology, 57, 14648-14660, 10.1021/acs.est.3c04411, 2023.

Kwok, R. H. F., Baker, K. R., Napelenok, S. L., & Tonnesen, G. S., Photochemical grid model implementation and application of VOC, NO x, and O3 source apportionment, Geoscientific Model Development, 8(1), 99-114, 10.5194/gmd-8-99-2015, 2015.

Li, J., Georgescu, M., Hyde, P., Mahalov, A., and Moustaoui, M.: Regional-scale transport of air pollutants: impacts of Southern California emissions on Phoenix ground-level ozone concentrations, Atmos. Chem. Phys., 15, 9345-9360, 10.5194/acp-15-9345-2015, 2015.

Li, P., Yang, Y., Wang, H., Li, S., Li, K., Wang, P., Li, B., and Liao, H.: Source attribution of near-surface ozone trends in the United States during 1995–2019, Atmos. Chem. Phys., 23, 5403-5417, 10.5194/acp-23-5403-2023, 2023.

Lu, C.-H., and J. S. Chang: On the indicator-based approach to assess ozone sensitivities and emissions features, J. Geophys. Res., 103, 3453–3462, doi:10.1029/97JD03128, 1998.

Ludewig, A., Kleipool, Q., Bartstra, R., Landzaat, R., Leloux, J., Loots, E., Meijering, P., van der Plas, E., Rozemeijer, N., Vonk, F., and Veefkind, P.: In-flight calibration results of the TROPOMI payload on board the Sentinel-5 Precursor satellite, Atmos. Meas. Tech., 13, 3561-3580, 10.5194/amt-13-3561-2020, 2020.

Lupaşcu, A. and Butler, T.: Source attribution of European surface O3 using a tagged O3 mechanism, Atmos. Chem. Phys., 19, 14535-14558, 10.5194/acp-19-14535-2019, 2019.

Lupaşcu, A., Otero, N., Minkos, A., and Butler, T.: Attribution of surface ozone to NOx and volatile organic compound sources during two different high ozone events, Atmos. Chem. Phys., 22, 11675-11699, 10.5194/acp-22-11675-2022, 2022.

Marsh, D. R., Mills, M. J., Kinnison, D. E., Lamarque, J.-F., Calvo, N., and Polvani, L. M.: Climate Change from 1850 to 2005 Simulated in CESM1(WACCM), Journal of Climate, 26, 7372-7391, https://doi.org/10.1175/JCLI-D-12-00558.1, 2013.

Martin, R. V., Fiore, A. M., & Van Donkelaar, A., Space-based diagnosis of surface ozone sensitivity to anthropogenic emissions, Geophysical Research Letters, 31(6), doi:10.1029/2004GL019416, 2004.

Maruhashi, J., Mertens, M., Grewe, V. and Dedoussi, I. C.: A multi-method assessment of the regional sensitivities between flight altitude and short-term O3 climate warming from aircraft NOx emissions, Environ. Res. Lett. 19 054007, https://doi.org/10.1088/1748-9326/ad376a, 2024.

McClure, C. D. and Jaffe, D. A.: Investigation of high ozone events due to wildfire smoke in an urban area, Atmospheric Environment, 194, 146-157, https://doi.org/10.1016/j.atmosenv.2018.09.021, 2018.

Mertens, M., Grewe, V., Rieger, V. S., & Jöckel, P.: Revisiting the contribution of land transport and shipping emissions to tropospheric ozone, Atmospheric Chemistry and Physics, 18, 5567–5588, https://doi.org/10.5194/acp-18-5567-2018, 2018.

Mertens, M., Kerkweg, A., Grewe, V., Jöckel, P., & Sausen, R.: Attributing ozone and its precursors to land transport emissions in Europe and Germany, Atmospheric Chemistry and Physics, 20, 7843–7873, https://doi.org/10.5194/acp-20-7843-2020, 2020.

Mertens, M., Jöckel, P., Matthes, S., Nützel, M., Grewe, V., and Sausen, R.: COVID-19 induced lower-tropospheric ozone changes, Environmental Research Letters, 16, 064005, 10.1088/1748-9326/abf191, 2021.

Miech, J. A., Herckes, P., Fraser, M. P., Arellano, A. F., Mirrezaei, M. A., and Guo, Y.: Evaluating Phoenix Metropolitan Area Ozone Behavior Using Ground-Based Sampling, Modeling, and Satellite Retrievals, Atmosphere, 15, 555, doi:10.3390/atmos15050555, 2024.

Mirrezaei, M. A., Arellano, A., Guo, Y., Roychoudhury, C., & Sorooshian, A.. Ozone production over arid regions: insights into meteorological and chemical drivers. Environmental Research Communications, 6(5), 051009, doi:10.1088/2515-7620/ad484c, 2024.

Nalam, A., Lupascu, A., Ansari, T., and Butler, T.: Regional and sectoral contributions of NOx and reactive carbon emission sources to global trends in tropospheric ozone during the 2000-2018 period, EGUsphere, 2024, 1-39, 10.5194/egusphere-2024-432, 2024.

Ninneman, M. and Jaffe, D. A.: The impact of wildfire smoke on ozone production in an urban area: Insights from field observations and photochemical box modeling, Atmospheric Environment, 267, 118764, https://doi.org/10.1016/j.atmosenv.2021.118764, 2021.

National Oceanic and Atmospheric Administration (NOAA) (2023). Hazard Mapping System Fire and Smoke Product. Retrieved from https://www.ospo.noaa.gov/Products/land/hms.html. Accessed on April 8, 2024.

Pfister, G. G., Walters, S., Emmons, L. K., Edwards, D. P., and Avise, J.: Quantifying the contribution of inflow on surface ozone over California during summer 2008, Journal of Geophysical Research: Atmospheres, 118, 12,282-212,299, https://doi.org/10.1002/2013JD020336, 2013.

Pfister, G. G., Emmons, L. K., Hess, P. G., Honrath, R., Lamarque, J.-F., Val Martin, M., Owen, R. C., Avery, M. A., Browell, E. V., Holloway, J. S., Nedelec, P., Purvis, R., Ryerson, T. B., Sachse, G. W., and Schlager, H.: Ozone production from the 2004 North American boreal fires, Journal of Geophysical Research: Atmospheres, 111, https://doi.org/10.1029/2006JD007695, 2006.

Rolph, G. D., Draxler, R. R., Stein, A. F., Taylor, A., Ruminski, M. G., Kondragunta, S., Zeng, J., Huang, H., Manikin, G., McQueen, J. T., & Davidson, P. M., Description and Verification of the NOAA Smoke Forecasting System: The 2007 Fire Season, Weather and Forecasting, 24(2), 361-378. https://doi.org/10.1175/2008WAF2222165.1, 2009.

Ruminski, M., Kondragunta, S., Monitoring fire and smoke emissions with the hazard mapping system, Proc. SPIE 6412, Disaster Forewarning Diagnostic Methods and Management, 64120B, https://doi.org/10.1117/12.694183, 2006.

Selimovic, V., Yokelson, R. J., McMeeking, G. R., and Coefield, S.: Aerosol Mass and Optical Properties, Smoke Influence on O3, and High NO3 Production Rates in a Western U.S. City Impacted by Wildfires, Journal of Geophysical Research: Atmospheres, 125, e2020JD032791, https://doi.org/10.1029/2020JD032791, 2020.

Shu, Q., Napelenok, S. L., Hutzell, W. T., Baker, K. R., Henderson, B. H., Murphy, B. N., and Hogrefe, C.: Comparison of ozone formation attribution techniques in the northeastern United States, Geosci. Model Dev., 16, 2303-2322, 10.5194/gmd-16-2303-2023, 2023.

Sillman, S.: The use of NOy, H2O2 and HNO3 as indicators for ozone-NOx-hydrocarbon sensitivity in urban locations, Journal of Geophysical Research: Atmospheres, 100, 14175-14188, 10.1029/94JD02953, 1995.

Sillman, S., D. He, C. Cardelino, and R. E. Imhoff: The use of photochemical indicators to evaluate ozone-NO_x-hydrocarbon sensitivity: Case studies from Atlanta, New York, and Los Angeles, J. Air Waste Manage. Assoc., 47, 642–652, DOI: 10.1080/10962247.1997.11877500, 1997.

Sorooshian, A., Arellano, A. F., Fraser, M. P., Herckes, P., Betito, G., Betterton, E. A., Braun, R. A., Guo, Y., Mirrezaei, M. A., and Roychoudhury, C.: Ozone in the Desert Southwest of the United States: A Synthesis of Past Work and Steps Ahead, ACS ES&T Air, 1, 62-79, 10.1021/acsestair.3c00033, 2024.

Thunis, P., Clappier, A., Tarrason, L., Cuvelier, C., Monteiro, A., Pisoni, E., Wesseling, J., Belis, C. A., Pirovano, G., Janssen, S., Guerreiro, C., and Peduzzi, E.: Source apportionment to support air quality planning: Strengths and weaknesses of existing approaches, Environment International, 130, 104825, https://doi.org/10.1016/j.envint.2019.05.019, 2019.

Tilmes, S., Lamarque, J. F., Emmons, L. K., Kinnison, D. E., Ma, P. L., Liu, X., Ghan, S., Bardeen, C., Arnold, S., Deeter, M., Vitt, F., Ryerson, T., Elkins, J. W., Moore, F., Spackman, J. R., and Val Martin, M.: Description and evaluation of tropospheric chemistry and aerosols in the Community Earth System Model (CESM1.2), Geosci. Model Dev., 8, 1395-1426, 10.5194/gmd-8-1395-2015, 2015.

Tonnesen, G.S., Dennis, R.L., Analysis of radical propagation efficiency to assess ozone sensitivity to hydrocarbons and NO x : 2. Long-lived species as indicators of ozone concentration sensitivity. J. Geophys. Res. Atmos. 105, 9227–9241, https://doi.org/10.1029/1999JD900372, 2000.

Turner, M. C., Jerrett, M., III, C. A. P., Krewski, D., Gapstur, S. M., Diver, W. R., Beckerman, B. S., Marshall, J. D., Su, J., Crouse, D. L., and Burnett, R. T.: Long-Term Ozone Exposure and Mortality in a Large Prospective Study, American Journal of Respiratory and Critical Care Medicine, 193, 1134-1142, 10.1164/rccm.201508-1633OC, 2016.

Urbanski, S. P., Hao, W. M., and Baker, S.: Chapter 4 Chemical Composition of Wildland Fire Emissions, in: Developments in Environmental Science, edited by: Bytnerowicz, A., Arbaugh, M. J., Riebau, A. R., and Andersen, C., Elsevier, 79-107, https://doi.org/10.1016/S1474-8177(08)00004-1, 2008.

USDA Forest Service: Tonto National Forest - Nature & Science, USDA Forest Service, https://www.fs.usda.gov/detail/tonto/learning/nature-science/?cid=fsbdev3_018777 (last access: 9 November 2024), 2024.

Van Geffen, J., Boersma, K. F., Eskes, H., Sneep, M., ter Linden, M., Zara, M., and Veefkind, J. P.: S5P TROPOMI NO2 slant column retrieval: method, stability, uncertainties and comparisons with OMI, Atmos. Meas. Tech., 13, 1315-1335, 10.5194/amt-13-1315-2020, 2020.

Wang, Y., and D. J. Jacob: Anthropogenic forcing on tropospheric ozone and OH since preindustrial times, J. Geophys. Res., 103, 31,123–31,135, doi:10.1029/1998JD100004, 1998.

Wang, Z. S., C.-J. Chien, and G. S. Tonnesen, Development of a tagged species source apportionment algorithm to characterize three-dimensional transport and transformation of precursors and secondary pollutants, J. Geophys. Res., 114, D21206, doi:10.1029/2008JD010846, 2009.

Whaley, C. H., K. Strong, D. B. A. Jones, T. W. Walker, Z. Jiang, D. K. Henze, M. A. Cooke, C. A. McLinden, R. L. Mittermeier, M. Pommier, et al.: Toronto area ozone: Long-term measurements and modeled sources of poor air quality events, J. Geophys. Res. Atmos., 120, 11,368–11,390, doi:10.1002/2014JD022984, 2015.

Wiedinmyer, C., Kimura, Y., McDonald-Buller, E. C., Emmons, L. K., Buchholz, R. R., Tang, W., Seto, K., Joseph, M. B., Barsanti, K. C., Carlton, A. G., and Yokelson, R.: The Fire Inventory from NCAR version 2.5: an updated global fire emissions model for climate and chemistry applications, Geosci. Model Dev., 16, 3873-3891, 10.5194/gmd-16-3873-2023, 2023.

Xu, L., Crounse, J. D., Vasquez, K. T., Allen, H., Wennberg, P. O., Bourgeois, I., Brown, S. S., Campuzano-Jost, P., Coggon, M. M., Crawford, J. H., DiGangi, J. P., Diskin, G. S., Fried, A., Gargulinski, E. M., Gilman, J. B., Gkatzelis, G. I., Guo, H., Hair, J. W., Hall, S. R., Halliday, H. A., Hanisco, T. F., Hannun, R. A., Holmes, C. D., Huey, L. G., Jimenez, J. L., Lamplugh, A., Lee, Y. R., Liao, J., Lindaas, J., Neuman, J. A., Nowak, J. B., Peischl, J., Peterson, D. A., Piel, F., Richter, D., Rickly, P. S., Robinson, M. A., Rollins, A. W., Ryerson, T. B., Sekimoto, K., Selimovic, V., Shingler, T., Soja, A. J., St. Clair, J. M., Tanner, D. J., Ullmann, K., Veres, P. R., Walega, J., Warneke, C., Washenfelder, R. A., Weibring, P., Wisthaler, A., Wolfe, G. M., Womack, C. C., and Yokelson, R. J.: Ozone chemistry in western U.S. wildfire plumes, Science Advances, 7, eabl3648, doi:10.1126/sciadv.abl3648, 2021.

Yeganeh, A. K., Momeni, M., Choi, Y., Park, J., and Jung, J.: A case study of surface ozone source contributions in the Seoul metropolitan area using the adjoint of CMAQ, Journal of the Air & Waste Management Association, null-null, 10.1080/10962247.2024.2361021, 2024.

Yokelson, R. J., Bertschi, I. T., Christian, T. J., Hobbs, P. V., Ward, D. E., and Hao, W. M.: Trace gas measurements in nascent, aged, and cloud-processed smoke from African savanna fires by airborne Fourier transform infrared spectroscopy (AFTIR), Journal of Geophysical Research: Atmospheres, 108, https://doi.org/10.1029/2002JD002322, 2003.

Zhang, L., Jacob, D. J., Boersma, K. F., Jaffe, D. A., Olson, J. R., Bowman, K. W., Worden, J. R., Thompson, A. M., Avery, M. A., Cohen, R. C., Dibb, J. E., Flock, F. M., Fuelberg, H. E., Huey, L. G., McMillan, W. W., Singh, H. B., and Weinheimer, A. J.: Transpacific transport of ozone pollution and the effect of recent Asian emission increases on air quality in North America: an integrated analysis using satellite, aircraft, ozonesonde, and surface observations, Atmos. Chem. Phys., 8, 6117–6136, https://doi.org/10.5194/acp-8-6117-2008, 2008.

Zhang, R., Cohan, A., Pour Biazar, A., and Cohan, D. S.: Source apportionment of biogenic contributions to ozone formation over the United States, Atmospheric Environment, 164, 8-19, https://doi.org/10.1016/j.atmosenv.2017.05.044, 2017.

Zhang, Y., Wen, X. Y., Wang, K., Vijayaraghavan, K., & Jacobson, M. Z.: Probing into regional O_3 and particulate matter pollution in the United States: 2. An examination of formation mechanisms through a process analysis technique and sensitivity study, Journal of Geophysical Research: Atmospheres, 114(D22), https://doi.org/10.1029/2009JD011900, 2009.

Zhang, Y., Zhao, Y., Li, J., Wu, Q., Wang, H., Du, H., Yang, W., Wang, Z., and Zhu, L.: Modeling Ozone Source Apportionment and Performing Sensitivity Analysis in Summer on the North China Plain, Atmosphere, 11, 992, doi:10.3390/atmos11090992, 2020.

Zhao, Y., Li, Y., Kumar, A., Ying, Q., Vandenberghe, F., & Kleeman, M. J., Separately resolving NOx and VOC contributions to ozone formation. Atmospheric Environment, 285, 119224, 10.1016/j.atmosenv.2022.119224, 2022.